

## AN HST/COS SURVEY OF THE LOW-REDSHIFT INTERGALACTIC MEDIUM. I. SURVEY, METHODOLOGY, AND OVERALL RESULTS

CHARLES W. DANFORTH, BRIAN A. KEENEY, EVAN M. TILTON, J. MICHAEL SHULL, JOHN T. STOCKE, MATTHEW STEVANS<sup>1</sup>, MATTHEW M. PIERI<sup>2</sup>, BLAIR D. SAVAGE<sup>3</sup>, KEVIN FRANCE, DAVID SYPHERS<sup>4</sup>, BRITTON D. SMITH<sup>5</sup>, JAMES C. GREEN, CYNTHIA FRONING<sup>1</sup>, STEVEN V. PENTON<sup>6</sup>, & STEVEN N. OSTERMAN<sup>7</sup>  
CASA, Department of Astrophysical & Planetary Sciences, University of Colorado, 389-UCB, Boulder, CO, USA 80309;  
danforth@colorado.edu

*Draft version September 4, 2018*

### ABSTRACT

We use high-quality, medium-resolution *Hubble Space Telescope*/Cosmic Origins Spectrograph (*HST*/COS) observations of 82 UV-bright AGN at redshifts  $z_{\text{AGN}} < 0.85$  to construct the largest survey of the low-redshift intergalactic medium (IGM) to date: 5138 individual extragalactic absorption lines in H I and 25 different metal-ion species grouped into 2611 distinct redshift systems at  $z_{\text{abs}} < 0.75$  covering total redshift pathlengths  $\Delta z_{\text{HI}} = 21.7$  and  $\Delta z_{\text{OVI}} = 14.5$ . Our semi-automated line-finding and measurement technique renders the catalog as objectively-defined as possible. The cumulative column-density distribution of H I systems can be parametrized  $dN(> N)/dz = C_{14}(N/10^{14} \text{ cm}^{-2})^{-(\beta-1)}$ , with  $C_{14} = 25 \pm 1$  and  $\beta = 1.65 \pm 0.02$ . This distribution is seen to evolve both in amplitude,  $C_{14} \propto (1+z)^{2.3 \pm 0.1}$ , and slope  $\beta(z) = 1.75 - 0.31z$  for  $z \leq 0.47$ . We observe metal lines in 418 systems, and find that the fraction of IGM absorbers detected in metals is strongly dependent on  $N_{\text{HI}}$ . The distribution of O VI absorbers appear to evolve in the same sense as the Ly $\alpha$  forest. We calculate contributions to  $\Omega_b$  from different components of the low- $z$  IGM and determine the Ly $\alpha$  decrement as a function of redshift. IGM absorbers are analyzed via a two-point correlation function in velocity space. We find substantial clustering of H I absorbers on scales of  $\Delta v = 50 - 300 \text{ km s}^{-1}$  with no significant clustering at  $\Delta v \gtrsim 1000 \text{ km s}^{-1}$ . Splitting the sample into strong and weak absorbers, we see that most of the clustering occurs in strong,  $N_{\text{HI}} \gtrsim 10^{13.5} \text{ cm}^{-2}$ , metal-bearing IGM systems. The full catalog of absorption lines and fully-reduced spectra is available via the Mikulski Archive for Space Telescopes (MAST) as a high-level science product at <http://archive.stsci.edu/prepds/igm/>.

*Subject headings:* astronomical databases: surveys—cosmological parameters—cosmology: observations—intergalactic medium—quasars: absorption lines

### 1. INTRODUCTION

The low-redshift intergalactic medium (IGM) holds many important clues to complete our understanding of cosmology. Even after nearly 14 Gyr of evolution, only a small fraction of baryonic matter has collapsed into luminous objects (galaxies, groups, clusters) while  $\sim 80\%$  or more still exists as a diffuse, often unvirialized IGM, the distribution and characteristics of which are only beginning to be measured (e.g., Shull, Smith, & Danforth 2012). Furthermore, there is a complicated and poorly understood interplay between the IGM, circumgalactic medium (CGM), and stars and gas in galaxies. These gaseous reservoirs provide raw material which is subsequently formed into stars and galaxies. These, in turn, enrich the IGM via outflows driven by super-

novae, radiation pressure, and active galactic nuclei (AGN Oppenheimer & Davé 2008; Smith et al. 2011).

Diffuse intergalactic gas is currently quite difficult to observe in emission (Frank et al. 2012; but see also Steidel et al. 2011; Martin et al. 2014a,b). The most sensitive method for detecting most of the gas is through absorption-line spectroscopy using bright background objects (typically AGN) to provide an ultraviolet continuum. The highest concentration of strong gas-diagnostic lines is in the rest-frame far-ultraviolet (FUV) band from  $\sim 2000 \text{ \AA}$  shortward to the Lyman edge at  $912 \text{ \AA}$ . Investigating the FUV at low redshift requires optimized spectrographs above Earth's UV-blocking atmosphere. Thus, there have been a series of space-based UV spectrographs, both as primary-science instruments on space-borne observatories (*Copernicus*, *International Ultraviolet Explorer*, *Hopkins Ultraviolet Telescope*, *Far-Ultraviolet Spectroscopic Explorer*) and instruments installed aboard the *Hubble Space Telescope* or *HST*: Faint Object Spectrograph (FOS), Goddard High-Resolution Spectrograph (GHRS), Space Telescope Imaging Spectrograph (STIS), and now the Cosmic Origins Spectrograph (COS).

COS is the fourth-generation UV spectrograph onboard *HST* and is optimized for medium-resolution ( $\lambda/\Delta\lambda \approx 18,000$ ,  $\Delta v \approx 17 \text{ km s}^{-1}$ ) spectroscopy of point

<sup>1</sup> Department of Astronomy, University of Texas at Austin, Austin, TX 78712

<sup>2</sup> A\*MIDEX, Aix Marseille Université, CNRS, LAM, UMR7326, Marseille, FR

<sup>3</sup> Department of Astronomy, University of Wisconsin, Madison, WI, USA, 53706

<sup>4</sup> East Washington University, Cheney, WA, USA, 99004

<sup>5</sup> Institute for Astronomy, University of Edinburgh, Royal Observatory, Edinburgh EH9 3HJ, UK

<sup>6</sup> Space Telescope Science Institute, Baltimore, MD, USA, 21218

<sup>7</sup> The Johns Hopkins University Applied Physics Lab, Laurel, MD, USA, 20723

sources in the 1135–1800 Å band (Green et al. 2012; Osterman et al. 2011). COS has an effective area that is an order of magnitude larger in the FUV ( $\lambda < 1800$  Å) than previous spectrographs. Furthermore, the excellent scattered light control and low background detectors of COS mean that fainter objects ( $F_\lambda \lesssim 10^{-14}$  erg cm $^{-2}$  s $^{-1}$  Å $^{-1}$ ) can be observed than with previous instruments, and higher quality spectra of bright targets can be obtained in much less time. In its first five years of science operations (Green et al. 2012), COS accumulated an unprecedented archive of hundreds of AGN spectra collected under a broad range of scientific programs from AGN physics to studies of the interstellar medium (ISM) in our own Galaxy. Regardless of their original scientific intent, many of these spectra are suitable for quasar absorption-line studies of the IGM.

In this paper, we build on the heritage of many previous low- $z$  IGM absorber catalogs from *HST*/FOS (Bahcall et al. 1993, 1996; Jannuzi et al. 1998; Weymann et al. 1998), *HST*/GHRS (Penton, Stocke, & Shull 2000), *FUSE* (Danforth & Shull 2005; Danforth et al. 2006), and *HST*/STIS (Penton, Stocke, & Shull 2004; Lehner et al. 2007; Danforth & Shull 2008; Tripp et al. 2008; Danforth et al. 2010a; Tilton et al. 2012). This current survey represents the largest sample of low- $z$  absorbers to date and is more sensitive than previous studies in most cases. It was designed to be a general-purpose survey with applications to a wide variety of extragalactic astrophysics: 82 extragalactic sight lines covering a combined redshift pathlength in H I of  $\Delta z = 21.7$ , 5138 intergalactic absorption lines comprising 2611 distinct redshift systems, and detections of 25 different metal-ion species. We describe the sample selection criteria, data reduction methods, and semi-automated measurement techniques in Section 2. We present the catalog and substantial electronic resources available to users of the survey in Section 3. Overall results from the survey are given in Section 4. In Section 5, we present some of the more detailed findings from the survey, including the evolution of H I and metals in the IGM at  $z \leq 0.47$  and the radial-velocity clustering properties of IGM absorbers (the two-point correlation function). Important survey parameters, fitted quantities, and initial findings are summarized in Section 6.

## 2. DATA ANALYSIS

### 2.1. Sight Line Selection

In the past five years, over 400 extragalactic targets have been observed with COS. The main objective of this project is to develop a comprehensive, statistical catalog of intervening absorbers in the low-redshift universe, in particular weak H I and metal-line systems. Obtaining high signal-to-noise data was our first priority in choosing which targets to include, which precludes many of the archival datasets. With a few exceptions, we include only spectra with a typical signal-to-noise of  $S/N \gtrsim 15$  per ( $\sim 17$  km s $^{-1}$ ) COS resolution element in the Ly $\alpha$  forest (see Keeney et al. 2012, for full discussion of the achievable  $S/N$  in COS data).

Secondly, we require reasonably distant targets to maximize the redshift pathlength probed by each sight line. Nearby AGN, particularly Seyfert galaxies, are typically

bright and often have exquisite spectra, but their available IGM pathlength is short and often contaminated by absorption intrinsic to the AGN. We require a sight line to have  $\Delta z_{\text{Ly}\alpha} \geq 0.05$  of unobstructed pathlength for inclusion in our survey. Conversely, high- $z$  targets sample long IGM pathlengths, but they often suffer from a high line density that makes line identification difficult. The two moderate-resolution FUV channels of COS (G130M and G160M) are only sensitive to H I absorption through Ly $\alpha$  at  $z \lesssim 0.47$  and through Ly $\beta$  and higher-order Lyman transitions at  $0.1 \lesssim z \lesssim 0.9$ . Thus we set an upper limit on source redshift of  $z_{\text{AGN}} < 0.9$ . Similarly, we concentrate on AGN observed with both the G130M and G160M gratings for the longest possible wavelength coverage. We augment the target list with a set of G130M-only observations of targets at  $z \lesssim 0.2$  where the entire Ly $\alpha$  forest falls within the G130M grating.

The COS FUV archive also contains  $\gtrsim 130$  extragalactic sight lines observed with the low-resolution ( $\Delta v \gtrsim 100$  km s $^{-1}$ ) G140L grating. While these data are often of higher quality than those from IUE or *HST*/FOS or low-resolution modes of GHRS or STIS, they are sensitive only to the strongest intervening absorbers, and we have not utilized them in this survey. However, these low-resolution and/or low-S/N data are useful for studies of AGN continua (e.g. Shull, Stevans, & Danforth 2012; Stevans et al. 2014), for surveys of strong absorption lines, and as flux-qualification observations for future medium-resolution observations.

AGN with strong absorption lines (BALs, mini-BALs) were not explicitly excluded from the survey. There are a few AGN with strong intrinsic absorption (e.g., RBS 542), but these systems are not on the level of a BAL or mini-BAL. In any case, absorption obviously intrinsic to the absorber was excluded from analysis (as discussed in S2.4.2).

To constitute our survey, we selected 82 AGN sight lines from the archive which met these criteria; 68 were observed with both FUV medium-resolution gratings (1135 – 1800 Å at  $\sim 17$  km s $^{-1}$  resolution) in the redshift range  $0.058 \leq z_{\text{AGN}} \leq 0.852$  and an additional 14 AGN at  $0.07 \leq z_{\text{AGN}} \leq 0.2$  had coverage in G130M only (1135 – 1450 Å). Astronomical target information is presented in Table 1. Most of the AGN observed in Cycles 18–20 under the Guaranteed Time Observation programs (GTO; PI-Green) are included, along with numerous archival datasets collected under various Guest Observer programs. Observational and programmatic details are presented in Table 2.

Individual exposures for each target were obtained from the Mikulski Archive for Space Telescopes (MAST). We start with `x1d.fits` files (individual exposures reduced to one-dimensional spectra) processed uniformly by the pipeline software circa mid-2014<sup>8</sup>. All exposures of each sight line were combined to maximize the  $S/N$  of each spectrum. The calibrated, one-dimensional spectra for each target were coadded into a continuous spectrum, usually over the useful range  $\sim 1140 - 1790$  Å employing a custom IDL procedure developed and extensively tested at University of Colorado.

<sup>8</sup> <http://www.stsci.edu/hst/cos/pipeline/CALCOSReleaseNotes/notes/>

TABLE 1  
HST/COS SIGHT LINES

Sight Line	R.A. (J2000)	Dec. (J2000)	$z_{\text{AGN}}$	Flux <sup>a</sup>	AGN type
PHL 2525	00 00 24.42	-12 45 47.8	0.1990	17.7	QSO
PG 0003+158	00 05 59.24	+16 09 49.0	0.4509	7.7	Sy1.2
PG 0026+129	00 29 13.71	+13 16 04.0	0.1420	19.1	Sy1
QSO 0045+3926	00 48 18.98	+39 41 11.6	0.1340	9.3	Sy1
HE 0056-3622	00 58 37.39	-36 06 05.0	0.1641	17.3	Sy1
RBS 144	01 00 27.13	-51 13 54.5	0.0628	22.1	Sy1
B0117-2837	01 19 35.70	-28 21 31.4	0.3489	11.6	Sy1
Ton S210	01 21 51.51	-28 20 57.8	0.1160	35.9	Sy1
HE 0153-4520	01 55 13.20	-45 06 12.0	0.4510	15.8	QSO
PG 0157+001	01 59 50.25	+00 23 41.3	0.1631	20.4	Sy1.5
3C 57	02 01 57.16	-11 32 33.1	0.6705	6.6	Sy1.2
3C 66A	02 22 39.61	+43 02 07.8	>0.3347	6.8	BL Lac
HE 0226-4110	02 28 15.19	-40 57 14.6	0.4934	21.4	Sy1
HE 0238-1904	02 40 32.50	-18 51 51.0	0.6310	14.0	QSO
UKS0242-724	02 43 09.60	-72 16 48.4	0.1018	10.3	Sy1.2
PKS 0405-123	04 07 48.43	-12 11 36.7	0.5740	32.1	Sy1.2
RBS 542	04 26 00.70	-57 12 01.8	0.1040	33.1	Sy1.5
HE 0435-5304	04 36 50.80	-52 58 49.0	0.4300	2.5	QSO
RX J0439.6-5311	04 39 38.64	-53 11 31.6	0.2430	3.5	Sy1
RX J0503.1-6634	05 03 03.93	-66 33 45.9	0.0640	6.4	Sy1
PKS 0552-640	05 52 24.50	-64 02 10.8	0.6800	11.1	AGN
PKS 0558-504	05 59 47.39	-50 26 51.9	0.1372	28.1	NLSy1/FSRQ
IRAS L06229-6434	06 23 07.68	-64 36 20.7	0.1290	8.0	FSRQ
PKS 0637-752	06 35 46.50	-75 16 16.8	0.6500	8.0	FSRQ
S5 0716+714	07 21 53.45	+71 20 36.4	>0.2315	24.3	BL Lac
SDSS J080908.13+461925	08 09 08.14	+46 19 25.7	0.6563	7.2	QSO
PG 0804+761	08 10 58.61	+76 02 41.6	0.1000	79.6	Sy1
PG 0832+251	08 35 35.80	+24 59 41.0	0.3298	3.5	QSO
PG 0838+770	08 44 45.26	+76 53 09.5	0.1310	8.5	Sy1
PG 0844+349	08 47 42.45	+34 45 04.4	0.0640	25.5	Sy1
Mrk 106	09 19 55.36	+55 21 37.4	0.1230	11.4	Sy1
SDSS J092554.43+453544	09 25 54.44	+45 35 44.5	0.3295	5.1	QSO
SDSS J092909.79+464424	09 29 09.78	+46 44 24.0	0.2400	11.5	QSO
SDSS J094952.91+390203	09 49 52.93	+39 02 03.8	0.3656	7.8	QSO
RXS J09565-0452	09 56 30.18	-04 53 17.0	0.1550	4.6	Sy1
PG 0953+414	09 56 52.41	+41 15 22.1	0.2341	38.1	QSO
PG 1001+291	10 04 02.59	+28 55 35.2	0.3297	10.6	Sy1
FBQS J1010+3003	10 10 00.70	+30 03 22.0	0.2558	2.5	QSO
Ton 1187	10 13 03.20	+35 51 23.0	0.0789	17.3	Sy1.2
PG 1011-040	10 14 20.68	-04 18 40.5	0.0583	16.2	Sy1.2
1ES 1028+511	10 31 18.50	+50 53 36.0	0.3604	2.6	BL Lac
1SAX J1032.3+5051	10 32 16.10	+50 51 20.0	0.1731	1.1	AGN
PG 1048+342	10 51 43.90	+33 59 26.7	0.1671	5.9	Sy1
PG 1049-005	10 51 51.48	-00 51 17.6	0.3599	9.2	Sy1.5
PMN J1103-2329	11 03 37.60	-23 29 30.0	0.1860	2.1	BL Lac/FSRQ
HS 1102+3441	11 05 39.80	+34 25 34.4	0.5088	3.6	QSO
SBS 1108+560	11 11 32.20	+55 47 26.0	0.7666	4.9	QSO
PG 1115+407	11 18 30.30	+40 25 54.0	0.1546	10.5	Sy1
PG 1116+215	11 19 08.60	+21 19 18.0	0.1763	45.7	Sy1
PG 1121+422	11 24 39.18	+42 01 45.0	0.2250	7.4	Sy1
SBS 1122+594	11 25 53.79	+59 10 21.6	0.8520	2.7	QSO
Ton 580	11 31 09.50	+31 14 05.0	0.2895	9.5	Sy1/FSRQ
3C 263	11 39 56.99	+65 47 49.2	0.6460	10.4	FR2/Sy1.2
PG 1216+069	12 19 20.93	+06 38 38.5	0.3313	12.3	NLSy1
PG 1222+216	12 24 54.45	+21 22 46.3	0.4320	17.0	Blazar
3C 273	12 29 06.70	+02 03 08.7	0.1583	461.5	FSRQ/Sy1.0
Q 1230+0115	12 30 50.00	+01 15 21.5	0.1170	36.3	NLSy1
PG 1229+204	12 32 03.61	+20 09 29.4	0.0630	19.2	Sy1
PG 1259+593	13 01 12.90	+59 02 07.0	0.4778	15.3	Sy1
PKS 1302-102	13 05 33.00	-10 33 19.0	0.2784	14.9	FSRQ/Sy1.2
PG 1307+085	13 09 47.01	+08 19 48.3	0.1550	25.0	Sy1.2
PG 1309+355	13 12 17.75	+35 15 21.1	0.1829	10.1	QSO
SDSS J135712.61+170444	13 57 12.60	+17 04 44.0	0.1500	4.7	QSO
PG 1424+240	14 27 00.39	+23 48 00.0	>0.6035	15.2	BL Lac
PG 1435-067	14 38 16.15	-06 58 20.7	0.1260	16.2	QSO
Mrk 478	14 42 07.47	+35 26 23.0	0.0791	26.4	NLSy1
Ton 236	15 28 40.60	+28 25 29.7	0.4500	6.1	Sy1.2
1ES 1553+113	15 55 43.04	+11 11 24.4	>0.4140	15.9	BL Lac/FSRQ
Mrk 876	16 13 57.20	+65 43 010.0	0.1290	39.5	Sy1
PG 1626+554	16 27 56.12	+55 22 31.5	0.1330	22.8	Sy1
H 1821+643	18 21 57.30	+64 20 36.0	0.2968	53.0	Sy1.2
PKS 2005-489	20 09 25.39	-48 49 53.7	0.0710	22.3	BL Lac
Mrk 1513	21 32 27.92	+10 08 18.7	0.0630	17.5	Sy1.5
RX J2154.1-4414	21 54 51.06	-44 14 06.0	0.3440	9.8	Sy1
PHL 1811	21 55 01.50	-09 22 25.0	0.1920	56.2	NLSy1

TABLE 1 — *Continued*

Sight Line	R.A. (J2000)	Dec. (J2000)	$z_{\text{AGN}}$	Flux <sup>a</sup>	AGN type
PKS 2155–304	21 58 52.07	-30 13 32.1	0.1165	73.1	BL Lac
RBS 1892	22 45 20.31	-46 52 11.8	0.2000	20.3	Sy1
IRAS F22456–5125	22 48 41.20	-51 09 53.2	0.1000	19.3	Sy1.5
MR 2251–178	22 54 05.88	-17 34 55.3	0.0640	34.3	Sy1.5
PMN J2345–1555	23 45 12.46	-15 55 07.8	0.6210	7.0	F5RQ
PG 2349–014	23 51 56.12	-01 09 13.1	0.1737	29.8	Sy1.2
H 2356–309	23 59 07.93	-30 37 40.9	0.1651	1.8	BL Lac

<sup>a</sup> Median observed continuum flux in the COS/FUV band in units of  $10^{-15} \text{ erg cm}^{-2} \text{ s}^{-1} \text{ \AA}^{-1}$ .

TABLE 2  
COS OBSERVATION DETAILS

Sight Line Name	Obs. Date (year-mo)	Exp. (ksec) (G130M)	S/N (G130M) <sup>a</sup>	Exp. (ksec) (G160M)	S/N (G160M) <sup>a</sup>	PI Name	Program Number
PHL 2525	2012-10	2.1	22	2.8	15	Fox	12604
PG 0003+158	2011-10	10.4	27	10.9	22	Green	12038
PG 0026+129	2011-10	1.9	21	...	...	Veilleux	12569
QSO 0045+3926	2009-10	13.5	40	17.2	31	Rich	11632
	2010-09					Arav	11686
HE 0056–3622	2012-07	5.0	32	5.7	20	Fox	12604
RBS 144	2012-04	2.4	26	3.0	19	Fox	12604
B0117–2837	2011-06	5.2	28	8.5	23	Thom	12204
Ton S210	2011-06	5.0	49	5.5	32	Thom	12204
HE 0153–4520	2009-12	5.2	30	5.9	23	Green	11541
PG 0157+001	2012-01	1.8	21	...	...	Veilleux	12569
3C 57	2011-08	11.0	29	8.7	17	Green	12038
3C 66A	2012-11	12.6	27	7.2	17	Stocke	12863
	2012-11					Furniss	12863
HE 0226–4110	2010-02	6.8	41	7.8	26	Green	11541
HE 0238–1904	2009-12	6.5	30	7.5	26	Green	11541
UKS0242–724	2011-06	2.1	20	3.2	14	Misawa	12263
PKS 0405–123	2009-08	24.2	76	11.1	35	Noll	11508
	2009-12					Green	11541
RBS 542	2010-06	20.4	67	15.9	41	Howk	11692
	2010-06					Arav	11686
HE 0435–5304	2010-04	8.4	16	8.9	10	Green	11520
RX J0439.6–5311	2010-02	8.2	21	8.9	12	Green	11520
RX J0503.1–6634	2010-09	4.7	21	3.9	12	Howk	11692
PKS 0552–640	2009-12	9.3	26	8.3	22	Howk	11692
PKS 0558–504	2010-05	1.1	20	0.7	9	Howk	11692
IRAS L06229–6434	2009-12	8.7	34	8.0	22	Howk	11692
PKS 0637–752	2009-12	9.6	26	8.7	18	Howk	11692
S5 0716+714	2011-12	6.0	41	8.3	32	Green	12025
SDSS J080908.13+461925	2010-10	3.1	17	5.0	14	Tumlinson	12248
PG 0804+761	2010-06	5.5	53	6.3	47	Arav	11686
PG 0832+251	2011-04	6.1	15	6.8	13	Green	12025
PG 0838+770	2009-09	8.9	34	6.3	18	Green	11520
PG 0844+349	2012-03	1.9	23	...	...	Veilleux	12569
Mrk 106	2011-05	6.5	32	7.6	21	Green	12029
SDSS J092554.43+453544	2010-10	4.4	17	7.1	16	Tumlinson	12248
SDSS J092909.79+464424	2010-10	2.4	20	2.9	14	Tumlinson	12248
SDSS J094952.91+390203	2010-09	2.3	16	2.8	13	Tumlinson	12248
RXS J09565–0452	2010-10	7.7	20	...	...	Wakker	12275
PG 0953+414	2011-10	4.8	42	5.6	30	Green	12038
PG 1001+291	2012-03	6.2	26	6.8	21	Green	12038
FBQS J1010+3003	2011-05	10.8	20	10.8	11	Green	12025
Ton 1187	2011-01	2.0	19	...	...	Wakker	12275
PG 1011–040	2010-03	5.4	34	4.7	22	Green	11524
1ES 1028+511	2011-05	14.7	23	14.6	13	Green	12025
1SAX J1032.3+5051	2011-10	11.4	12	11.3	7	Green	12025
PG 1048+342	2011-04	7.8	25	11.0	18	Green	12024
PG 1049–005	2011-06	2.3	15	2.8	14	Tumlinson	12248
PMN J1103–2329	2011-07	13.3	19	13.3	11	Green	12025
HS 1102+3441	2010-01	11.4	21	11.3	15	Green	11541
SBS 1108+560	2011-05	8.4	5	8.9	15	Green	12025
PG 1115+407	2010-06	5.1	26	5.7	17	Green	11519
PG 1116+215	2011-10	4.7	43	5.5	32	Green	12038
PG 1121+422	2011-04	5.0	23	5.8	14	Green	12024
SBS 1122+594	2009-11	9.9	17	10.5	13	Green	11520
Ton 580	2010-01	4.9	24	5.6	19	Green	11519
3C 263	2010-01	15.4	40	18.0	28	Green	11541

TABLE 2 — *Continued*

Sight Line Name	Obs. Date (year-mo)	Exp. (ksec) (G130M)	$S/N$ (G130M) <sup>a</sup>	Exp. (ksec) (G160M)	$S/N$ (G160M) <sup>a</sup>	PI Name	Program Number
PG 1216+069	2012-02	5.1	27	5.6	21	Green	12025
PG 1222+216	2013-12	3.4	21	7.7	26	Stocke	13008
3C 273	2012-04	4.0	78	...	...	Green	12038
Q 1230+0115	2010-07	11.0	50	11.0	40	Arav	11686
PG 1229+204	2012-04	1.9	18	...	...	Veilleux	12569
PG 1259+593	2010-04	9.2	39	11.2	29	Green	11541
PKS 1302–102	2011-08	6.0	31	6.9	23	Green	12038
PG 1307+085	2012-06	1.8	23	...	...	Veilleux	12569
PG 1309+355	2011-12	1.9	15	...	...	Veilleux	12569
SDSS J135712.61+170444	2011-06	4.2	18	6.8	12	Tumlinson	12248
PG 1424+240	2012-04	3.8	24	7.9	25	Stocke	12612
PG 1435–067	2012-02	1.9	20	...	...	Veilleux	12569
Mrk 478	2012-01	1.9	21	...	...	Veilleux	12569
Ton 236	2011-09	6.6	20	9.4	17	Green	12038
1ES 1553+113	2009-09	10.8	38	11.9	30	Green	11520
	2011-07					Green	12025
Mrk 876	2010-04	12.6	59	11.8	42	Arav	11686
	2010-04					Green	11524
PG 1626+554	2011-06	3.3	33	4.3	22	Green	12029
H 1821+643	2009-07	12.0	59	0.5	14	Hartig	11484
	2012-07					Green	12038
PKS 2005–489	2009-09	2.5	28	1.9	17	Green	11520
Mrk 1513	2010-10	5.5	33	4.8	23	Green	11524
RX J2154.1–4414	2010-06	8.2	32	8.5	25	Green	11541
PHL 1811	2010-10	3.5	42	3.1	27	Green	12038
PKS 2155–304	2012-07	4.6	49	...	...	Green	12038
RBS 1892	2012-07	2.2	23	2.9	16	Fox	12604
IRAS F22456–5125	2010-06	15.1	52	11.9	31	Arav	11686
MR 2251–178	2011-09	4.6	38	5.4	31	Green	12029
PMN J2345–1555	2013-08	4.1	17	7.6	16	Stocke	13008
PG 2349–014	2011-10	1.8	25	...	...	Veilleux	12569
H 2356–309	2013-06	17.0	19	...	...	Fang	12864

<sup>a</sup> Median  $S/N$  per resolution element in the G130M and G160M channels.

## 2.2. Data Reduction and Processing

The default pipeline software that produces the `x1d.fits` files is capable of combining *HST*/COS FUV data taken at multiple FP-POS positions for a single CENWAVE, but it does not combine data across multiple CENWAVE positions nor does it combine data taken with the G130M and G160M gratings. Our IDL procedure `coadd_x1d` was written to serve this purpose, as were several other routines used by other groups, including the `counts_coadd` code used by the COS Halos and COS Dwarfs teams (e.g., Tumlinson et al. 2011; Werk et al. 2014; Bordoloi et al. 2014) and the `coscombine` code used by the Wisconsin group (e.g., Savage et al. 2014; Fox et al. 2015; Wakker et al. 2015). While all of these routines share the common goal of optimally combining data taken across multiple FP-POS and CENWAVE positions and gratings, they do have some differences in implementation, including the procedure by which individual exposures are cross-correlated and interpolated onto a common wavelength scale. However, the primary philosophical difference between these codes is in the units of their output. Our procedure, `coadd_x1d`, preserves the flux units of the input `x1d.fits` files, while the other two routines create spectra whose fluxes are in units of counts/sec, which simplifies the Poissonian error treatment. Since the `x1d.fits` files contain the flux, net counts, and gross counts as a function of wavelength for each exposure, our procedure uses the gross counts at a given wavelength to determine

a Poissonian uncertainty that is valid in the low-count regime (e.g., Gehrels 1986). This uncertainty array is then multiplied by an empirical sensitivity function, which is given by the ratio of the flux and net counts arrays, to convert the uncertainty values into the units of the flux array before proceeding with coaddition.

Danforth et al. (2010b) describe the basic algorithm of `coadd_x1d`, but many refinements have been made over the intervening years. The revised coaddition algorithm proceeds sequentially as follows:

1. The `x1d.fits` files are opened, loaded into input arrays, and examined individually.
2. The data quality (DQ) flags from the `x1d.fits` files are parsed to remove bad pixels. Pixels with some DQ values<sup>9</sup> are instead de-weighted by artificially increasing their uncertainty so that they contribute half as much to the coadded spectrum than they otherwise would.
3. The input data are binned (i.e., Nyquist sampled) if requested by the user. At this stage the exposure-level uncertainties are optionally modified to incorporate the non-Poissonian noise characterized in Keeney et al. (2012), ensuring that the uncertainty values reflect the RMS fluctuations about

<sup>9</sup> A particular DQ flag is set by flipping one of 15 bits in an unsigned integer. Of these 15 bits, nine are handled identically by `coadd_x1d` and the default `calcos` pipeline, three are handled more leniently by `coadd_x1d` (pixels with DQ values of 8, 16, 32 are rejected by `calcos` but only de-weighted by `coadd_x1d`), and three are handled more strictly by `coadd_x1d` (DQ values of 4, 1024, 4096 are de-weighted by `coadd_x1d` and ignored by `calcos`).

the continuum level. While neither of these steps are default behaviors of `coadd_x1d`, all data for this paper were processed with these flags.

4. A reference exposure is chosen and all other exposures are aligned to it using cross correlation in the regions surrounding strong ISM lines (one cross-correlation feature per detector segment). This procedure provides a first-order wavelength alignment between exposures, which are in the heliocentric frame output by the `CALCOS` pipeline. However, there may be residual shifts of up to a few resolution elements at different wavelengths in the coadded data (Tripp et al. 2008; Savage et al. 2014; Wakker et al. 2015).
5. The flux level of each exposure is scaled to match the flux in the reference exposure, and uncertainty is scaled by this same factor. The majority (75/82) of the AGN sight lines were observed during only a single epoch, and the changes in source brightness over the observing period tended to be negligible (only 8% of exposures required a flux scaling of greater than 10%; however, see Danforth et al. 2013, for a dramatic counter-example). Observations at different epochs occasionally have significantly different fluxes; these cases are scaled to match the first data epoch. We assume no changes in spectral shape or absorption/emission properties between epochs or exposures. Absolute velocity calibration of arbitrary *HST*/COS data to better than  $\sim 10 \text{ km s}^{-1}$  is problematic owing to the precise location of the spectrum on the detector and the complicated wavelength solution.
6. The individual exposures are interpolated onto a common wavelength scale. It is important to use nearest-neighbor interpolation (i.e., shift and add) to minimize the non-Poissonian noise introduced by the coaddition process (e.g., correlated noise from linear interpolation; Keeney et al. 2012).
7. Combine the individual exposures using one of several weighting methods (arithmetic mean, exposure-time weighting, inverse-variance weighting, or signal-to-noise weighting). We use the default inverse-variance weighting for this analysis.
8. Finally, the quantities of interest (wavelength, coadded flux, and coadded uncertainty at a minimum) are returned to the user.

Next, continua were fitted to each of the coadded data sets using a semi-automated continuum-fitting technique developed for fitting optical SDSS spectra (Pieri et al. 2014) and adapted for use in higher-resolution FUV datasets. First, the spectra were split into segments of 5–15 Å width (width of the bins was adjusted qualitatively based on how smooth the AGN continuum was and the density of strong absorption features). Continuum pixels within each segment were identified as those for which the flux-to-error ratio was less than  $1.5\sigma$  below the median flux/error value for all the pixels in the segment. Thus, absorption lines (flux lower than the segment median) were excluded, as were regions of unusually strong noise

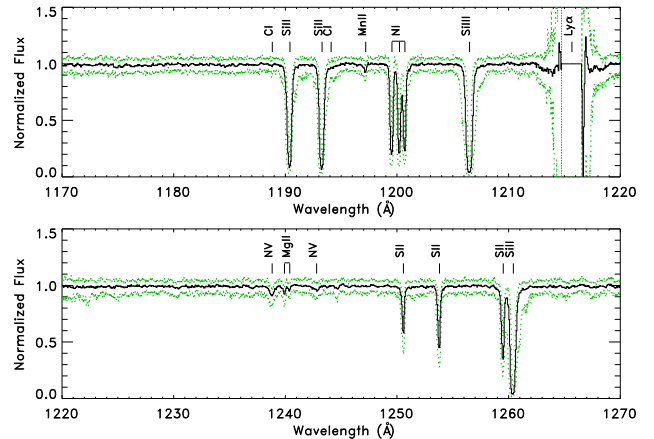


FIG. 1.— Median-combined “Galactic foreground” coaddition of 82 normalized AGN spectra in our survey reveals the Galactic foreground absorption present in most extragalactic spectra. A line-dense 100 Å spectral region near the blue end of the COS/FUV spectral range is shown. Dotted curves show  $\pm 1\sigma$  normalized flux values in the sample at each wavelength. Identified Galactic absorption lines are labeled. The full spectrum is available at <http://archive.stsci.edu/prepds/igm/>.

(error higher than segment average). The process was iterated until minimal change occurred in the population of continuum pixels between one iteration and the next, or until only 10% of the original pixels in the segment remained classified as continuum. The median value of the continuum pixels was then recorded as a continuum flux node for the 5–15 Å segment and a spline function was fitted between the nodes.

The continuum fit of each spectrum was then checked manually and adjusted as needed. The continuum identification and spline-fitting processes worked well in regions where continua varied smoothly, but it was often poor in regions of sudden change. For instance, spline fits perform poorly at the sharp peaks of emission lines (cusps), in the Galactic Ly $\alpha$  absorption trough (1210–1220 Å), at the absorption edge of partial Lyman limit systems (Stevans et al. 2014), and at the edges of the detectors ( $\lambda \lesssim 1140 \text{ Å}$ ,  $\lambda \gtrsim 1790 \text{ Å}$ ). The spline fits in these regions were replaced by piecewise-continuous, low-order Legendre polynomial fits.

### 2.3. Absorber Identification and Measurement

A weakness in previous quasar absorption-line surveys (e.g., Penton, Stocke, & Shull 2000; Danforth & Shull 2008, hereafter DS08) was the subjective nature of identifying absorption features in normalized data. We partially corrected for this bias here by implementing an automated line-finding and measurement algorithm modeled on that used in the FOS Key Project work (Schneider et al. 1993). We believe this yields a more objectively-defined catalog of absorption lines.

First, we generated a “line-less error vector”  $\bar{\sigma}(\lambda)$  by interpolating the error  $\sigma(\lambda)$  in regions defined as continuum over those identified as non-continuum during the continuum fitting process. We calculated an equivalent width vector  $W(\lambda)$  by convolving the normalized flux pixels with a representative line profile. The line profile is the COS line spread function (Kriss 2011) convolved with a Gaussian with Doppler parameter,  $b = 20 \text{ km s}^{-1}$ , typ-

ical of narrow absorption lines in the ISM and IGM. The error vector  $\bar{\sigma}(\lambda)$  was convolved with the same line spread function, and a crude significance-level vector was calculated as  $SL(\lambda) = W(\lambda)/\bar{\sigma}(\lambda)$ . Initial absorber locations were identified by finding local maxima in significance level where  $SL \geq 3$ . We repeated the procedure using broader convolved-Gaussian templates ( $b = 50 \text{ km s}^{-1}$  or  $100 \text{ km s}^{-1}$  typical of broad or blended absorption lines) although the line-finding technique is not sensitive to the exact choice of kernel width. Any additional line locations found with the broad kernels were added to the list.

Next, Voigt profiles convolved with the COS line spread function were fitted to the normalized data at each of the identified  $SL > 3$  locations. All lines were *initially* fitted as Ly $\alpha$ , and the fit parameters were allowed to vary over the range  $8 < b < 150 \text{ km s}^{-1}$ ,  $10 < \log N (\text{cm}^{-2}) < 16.5$ , and  $\Delta v = \pm 50 \text{ km s}^{-1}$ . Adjacent lines were fitted simultaneously. The significance level of each fit (Keeney et al. 2012) and a goodness-of-fit parameter similar to a reduced  $\chi^2$  value were determined for each component. (Note that, since noise features are correlated between pixels, this is not a formal reduced  $\chi^2$  measurement.) Highly significant lines ( $SL \geq 10$ ) with mediocre fit qualities were refitted with two components, and the resulting one- and two-component fits were compared with an  $F$ -test (Press et al. 1992). The two-component fit was adopted only if it was better than the single-component fit by more than  $5\sigma$ , chosen empirically based on a large sample of blended lines in the data.

The centroid wavelength,  $b$ -value, equivalent width, and column density (with uncertainties) of each feature were recorded in an initial line list along with the fit significance level and  $\bar{\chi}^2$ . Additionally, the local S/N per resolution element in the normalized data was determined as  $S/N \equiv 1/\sigma_r$  where  $\sigma_r$  is the RMS of continuum pixels when smoothed to a resolution element.

In the majority of cases, the fully-automated line-finding and measurement procedure produced acceptable fits. However, some automated line fits were deemed “pathological”, in cases when the solution represented the minimum  $\chi^2$  over the parameter search space, but the fit was clearly not representative of the absorption feature. The most common of these cases were fits to weak lines adjacent to strong features in which saturated pixels would drive the line profile to a spurious fit. Line measurements with  $\bar{\chi}^2 > 1$  were presented for manual refitting during the line identification process below, and components were often added or removed based on qualitative assessment.

The automated line-finding algorithm detected  $\sim 30$  very broad ( $b > 75 \text{ km s}^{-1}$ ), weak ( $3\text{-}4\sigma$ ) absorbers some of which are not subjectively obvious in the data but meet the  $> 3\sigma$  significance criterion. Some of these features were clearly suspect as regions of ambiguous continuum or statistical fluctuations in the noise and were rejected. However, an objective treatment of absorption features was one of the main drivers for our automated line-finding systems and we included most of them in the final line catalog. We caution users that they should interpret these features with a critical eye in any detailed analysis.

TABLE 3  
GALACTIC ABSORPTION LINES IN FAR-UV HST/COS SPECTRA

Ion	Strong Lines			Ref. <sup>a</sup>	Ion	Weak Lines		
	$\lambda$ (Å)	$f$				$\lambda$ (Å)	$f$	Ref. <sup>a</sup>
NI	1134.17 <sup>b</sup>	0.0146	1	Fe II	1142.37	0.0040	1	
NI	1134.41 <sup>b</sup>	0.0287	1	Fe II	1143.23	0.0192	1	
NI	1134.98 <sup>b</sup>	0.0416	1	CI	1157.91	0.0212	1	
Fe II	1144.94	0.0830	1	CI	1194.00	0.0124	1	
P II	1152.82	0.245	1	Mn II	1197.18	0.148	2	
Si II	1190.42	0.292	1	N V	1238.82	0.156	1	
Si II	1193.29	0.582	1	Mg II	1239.94	0.000621	3	
NI	1199.55 <sup>b</sup>	0.132	1	Mg II	1240.39	0.000351	3	
NI	1200.22 <sup>b</sup>	0.0869	1	N V	1242.80	0.0777	1	
NI	1200.71 <sup>b</sup>	0.0432	1	CI	1277.25	0.1314	4	
Si III	1206.50	1.63	1	CI	1280.14	0.0481	4	
HI Ly $\alpha$	1215.67 <sup>b</sup>	0.4164	1	Ni II	1317.22	0.0571	5	
S II	1250.58	0.00543	1	CI	1328.83	0.0899	4	
S II	1253.81	0.0109	1	C II	1347.24	0.153	1	
S II	1259.52	0.0166	1	Ni II	1370.13	0.0588	5	
Si II	1260.42	1.18	1	Ni II	1454.84	0.0323	6	
O I	1302.17 <sup>b</sup>	0.0480	1	Ni II	1467.76	0.0099	6	
Si II	1304.37	0.0863	1	CI	1560.31	0.1315	7	
C II	1334.53	0.128	1	Fe II	1611.20	0.0014	1	
C II*	1335.66	0.128	1	CI	1656.93	0.1488	7	
Si IV	1393.76	0.513	1	Ni II	1703.41	0.0060	6	
Si IV	1402.77	0.254	1	Ni II	1709.60	0.0324	6	
Si II	1526.71	0.133	1	Ni II	1741.55	0.0427	6	
C IV	1548.20	0.1899	1	Ni II	1751.91	0.0277	6	
C IV	1550.78	0.09475	1					
Fe II	1608.45	0.0577	1					
Al II	1670.79	1.74	1					

<sup>a</sup> Vacuum wavelengths and oscillator strength references: 1- Morton (2003), 2- Toner & Hibbert (2005), 3- Kelleher & Podobedova (2008), 4- Jenkins & Tripp (2001), 5- Jenkins & Tripp (2006), 6- Fedchak et al. (2000), 7- Jenkins & Tripp (2011)

<sup>b</sup> Geocoronal airglow is often associated with this transition in addition to Galactic absorption.

There are  $\sim 25$  strong absorption lines arising in the Milky Way ISM that present a foreground to every extragalactic absorption spectrum (Figure 1, Table 3). Another  $\sim 25$  weaker lines, particularly those of N V, C I, and Ni II, are seen in some of the sight lines and can be confused with IGM absorption. To characterize these, we performed a simple median-combined coaddition of all 82 normalized COS AGN spectra in the observed (heliocentric) frame. This ‘‘Galactic foreground’’ spectrum reaches a very high S/N ( $\sim 100$ ) and shows the foreground lines frequently present in the data. It is available on-line as a MAST high-level science product as described in Section 3. Since the relative strengths, centroids, and line widths of these Galactic lines vary from one sight line to another, the foreground spectrum cannot be used as a true Galactic flat field. However, it is useful for identifying individual absorption features as Galactic or intergalactic in nature and in masking regions of spectra which are insensitive to IGM absorption features.

Measured lines that are consistent with ISM features typically seen in FUV spectra are flagged as probable ISM absorption. If these lines are not subsequently re-identified as an IGM line or a blend of IGM and ISM features, they are ignored in the remainder of this analysis. Table 3 lists the commonly-seen Galactic absorption features in the  $1135 \text{ \AA} < \lambda < 1800 \text{ \AA}$  spectral range. We note that Table 3 is not a comprehensive list of all FUV transitions of reasonable strength; some lines would be visible in some spectra but for blending with a stronger, omnipresent ISM line (e.g., the weak C I 1260.74 line which, even when other comparable C I lines are seen, will always be blended with strong Si II 1260.42 absorption). High-velocity Galactic absorption present in many datasets ( $\Delta v \lesssim 500 \text{ km s}^{-1}$ ) is flagged by using the same ISM template offset by a constant velocity. ISM lines that have not been re-identified as IGM lines or blends are recorded in the line lists for completeness along with measured equivalent widths, but no attempt has been made to measure accurate column densities or detailed component structure for them.

The automatic line-fitting procedure assumed that all features were Ly $\alpha$  forest lines (statistically, the most common IGM line). However, this is not always the case. Line identification was by far the most time-intensive part of the process, since automation in this area was not reliable. After pathological fits were corrected and  $v \approx 0$  ISM lines were identified and flagged, the remaining lines were identified by a variety of means. For sight lines covering a long pathlength ( $\Delta z \gtrsim 0.15$ ), correlated absorption in multiple transitions of a species (e.g., H I Ly $\alpha$  and Ly $\beta$ ) was the most productive technique. For instance, overplotting  $z_{\text{Ly}\alpha} = (\lambda/1215.67\text{\AA}) - 1$  versus flux and  $z_{\text{Ly}\beta} = (\lambda/1025.72\text{\AA}) - 1$  versus flux shows correlated absorption at the redshift of any moderately-strong H I systems ( $N_{\text{HI}} \gtrsim 10^{14} \text{ cm}^{-2}$ ). Comparisons of Ly $\beta$ /Ly $\gamma$  reveal strong H I absorbers at  $z_{\text{abs}} > 0.47$  where Ly $\alpha$  has redshifted past the end of the COS/G160M detector. Occasionally, metal-ion doublet transitions O VI (1031.93, 1037.64  $\text{\AA}$ ) and C IV (1548.20, 1550.77  $\text{\AA}$ ) revealed IGM systems where H I absorption was weak, not present, or blended with other absorption lines. Identifying the redshifts of the strongest absorption systems

in this way allows us to identify single-transition metal ions (C III  $\lambda 977.02$ , Si III  $\lambda 1206.50$ , N III  $\lambda 989.80$ ) and other species in some cases (e.g., C II, Si II, O IV, etc.). *FUSE* data, where present, were used to help confirm these correlated absorber systems, but is not otherwise measured; see Tilton et al. (2012) for a complete list of *FUSE+HST/STIS* IGM absorbers. Ly $\alpha$  line fits were adjusted as needed and those lines identified as something other than Ly $\alpha$  were refitted manually with the appropriate atomic parameters.

Regardless of how it was identified, each extragalactic system redshift was checked for corresponding absorption in the transitions most commonly seen in the IGM: H I Ly $\alpha$ - $\delta$ , O VI, Si III/IV, C III/IV, N V; see Table 3 of DS08 for details. A small number of systems also showed absorption in additional ions (e.g., C II, Fe II/III, Si II, Ne VIII, O IV, N III, and higher-order Lyman lines).

### 2.3.1. Line Identification Ambiguities

Because Ly $\alpha$  1215.67  $\text{\AA}$  is typically the strongest transition in any diffuse IGM absorber, many low-column density systems are single-line identifications for which higher order Lyman transitions and metals are too weak to be observed. As in our previous papers, we assume that these are weak Ly $\alpha$  lines unless that assumption is inconsistent with either the source redshift ( $z_{\text{abs}} > z_{\text{AGN}}$  or  $z_{\text{abs}} < 0$ ), a non-detection upper limit in another transition, or a more plausible identification in another identified system.

We have identified all absorption features to the best of our abilities, but some ambiguities exist. Throughout, we assume that any system with more than one line is unambiguous. However, single-line identifications are still in the majority and, in principle present cases where the line identification is ambiguous. The majority ( $\sim 75\%$ ) of IGM systems consist of single Ly $\alpha$  absorbers without any confirming Ly $\beta$  or metal-ion detection at the same redshift. This uncertainty is greatest for the longer sight lines (higher  $z_{\text{AGN}}$ ) since there are more intervening systems and more possibilities for unusual metal-ion absorbers. Short pathlengths offer a more compact Ly $\alpha$  forest with fewer realistic possibilities for line identification; in such cases, Ly $\alpha$  is usually the only plausible identification. Nevertheless, a few of these single-line systems may be metal-line absorption from a different redshift or instrumental features.

At  $z \gtrsim 0.47$ , Ly $\alpha$  shifts beyond the red end of the COS G160M detector; thus there are 13  $z_{\text{AGN}} > 0.47$  sight lines with incomplete coverage of the Ly $\alpha$  forest. In these sight lines, some weak absorbers identified as Ly $\alpha$  at  $0.24 < z_{\text{abs}} < 0.47$  could instead be strong Ly $\beta$  systems at  $z > 0.47$ . For stronger lines, the  $z_{\text{abs}} > 0.47$  Ly $\beta$  interpretation can be ruled out with a Ly $\gamma$  upper limit (i.e., the predicted Ly $\gamma$  absorber is strong enough that it should appear in the data). However, there are  $\sim 40$  weak lines in our survey with this Ly $\alpha$ /Ly $\beta$  ambiguity. From the ratio of oscillator strengths and rest wavelengths, the column density ratio  $N_{\text{Ly}\beta}/N_{\text{Ly}\alpha} = (f\lambda)_{\text{Ly}\alpha}/(f\lambda)_{\text{Ly}\beta} = 6.2$  for a weak line of a given observed equivalent width. Since the frequency of H I absorbers  $\partial^2 \mathcal{N}(N)/\partial N \partial z \propto N^{-\beta}$  where  $\beta \approx 1.6$ , Ly $\beta$  absorbers should make up only  $6.2^{-1.6} = 5\%$  of the ambiguous sample or  $\sim 2/40$  weak Ly $\alpha$  absorbers at  $0.24 < z_{\text{abs}} < 0.47$  in 13 sight lines.

The inverse case (weak Ly $\alpha$  lines at  $z_{\text{abs}} < 0.47$  misidentified as Ly $\beta$  or Ly $\gamma$  at  $z_{\text{abs}} > 0.47$ ) should not be present in this survey, since we require any  $z_{\text{abs}} > 0.47$  absorber to be confirmed with detections in at least two transitions at that redshift (typically Ly $\beta$ +Ly $\gamma$  or metal-ion doublets).

### 2.3.2. Instrumental Features

As with any instrument, *HST*/COS suffers from a variety of instrumental artifacts which can masquerade as real spectral features. These include “gain sag”, areas of decreased sensitivity near detector edges, and fixed pattern noise. Use of quality flags in the coaddition process described above minimizes the impact of most of these effects, but some instrumental features are inevitably present in the data. Fixed pattern noise is the most common feature and manifests itself as small undulations across the face of an otherwise smooth continuum. Efforts to fully characterize this noise, much less correct for it, have proven elusive (Wakker et al. 2015). A small fraction of our weak absorption features are undoubtedly instrumental rather than real features.

## 2.4. IGM Absorber Analysis

### 2.4.1. Significance Levels

Absorption features are initially identified using the simple approximation for significance level as described above. During the fitting process, we use a more rigorous significance-level formula

$$SL = (S/N)_1 \frac{W_\lambda}{\Delta\lambda} \frac{1}{w(x_{\text{opt}})}, \quad (1)$$

where  $(S/N)_1$  is the signal-to-noise ratio per single pixel,  $W_\lambda$  is the equivalent width, and  $\Delta\lambda$  is the pixel width in Angstroms. The quantity  $w(x_{\text{opt}})$  is an empirical function that describes the correspondence between  $(S/N)_1$  and the signal-to-noise level for data binned to an optimal number of pixels  $x_{\text{opt}}$ . The parameter  $x_{\text{opt}}$  is a function of the observed wavelength and the Doppler  $b$ -parameter of the feature. Full details are given in equations (4), (7), and (9-11) of Keeney et al. (2012)<sup>10</sup>.

Throughout the analysis, we retain any features measured with  $SL > 3$ . However, even  $3\sigma$  features are statistically common; a typical COS spectrum covers approximately 8000 resolution elements between 1150 Å and 1800 Å. There could be  $\sim 20$  spurious  $3\sigma$  features with  $b$ -values typical of narrow absorbers in each COS/FUV spectrum given normally-distributed (Gaussian) noise. A more stringent  $4\sigma$  detection threshold should result in less than one spurious feature per spectrum.

The COS noise characteristics are poorly constrained and are not purely Gaussian in nature (Keeney et al. 2012). However, a  $4\sigma$  detection threshold will still result in fewer spurious detections than a  $3\sigma$  criterion; for this reason, we set the following criteria for inclusion in our catalog. Single-line detections must be  $\geq 4\sigma$ . However, if a  $4\sigma$  prior exists from another line detection, we relax the threshold to  $\geq 3\sigma$  for lines in other transitions at the same redshift. For example, a single weak absorber

measured at  $3.5\sigma$  would be rejected from the statistics, but retained in the line catalog. However, if the weak absorber can be interpreted as a metal line or higher-order Lyman transition of a stronger absorber, it would be accepted and used in later analysis. Practically, this means that the Ly $\alpha$  detection threshold is set at  $4\sigma$ , while the higher-order Lyman line and metal-line threshold is  $3\sigma$  since metal absorption is almost never seen without an H I prior. We use the same criteria for calculating the total pathlength  $\Delta z(N)$  observed at column density  $N$ .

### 2.4.2. Intrinsic Absorbers

Galactic features are easily identified as discussed above. However, absorption from intervening (IGM) gas can sometimes be difficult to differentiate from that arising from gas associated with the AGN host galaxy itself (intrinsic absorbers with  $z_{\text{abs}} \approx z_{\text{AGN}}$ ). There is no definitive way to identify an absorber as one or the other since AGN outflow features have been observed at very large relative velocities. We automatically flag any absorber with  $\Delta v = (cz_{\text{AGN}} - cz_{\text{abs}})/(1 + z_{\text{AGN}}) \leq 1500 \text{ km s}^{-1}$  as a possible intrinsic system. The exceptions to the  $\Delta v < 1500 \text{ km s}^{-1}$  proximity rule are the four BL Lacertae objects in the sample. These objects (1ES 1553+113, 3C 66A, S5 0716+714, and PG 1424+240) have source redshift lower limits defined by observed narrow IGM absorbers. Since outflows are sometimes seen at higher velocities, we also manually check any metal-line systems at  $1500 < \Delta v < 5000 \text{ km s}^{-1}$  for obvious AGN-intrinsic properties (e.g., Dunn et al. 2007; Ganguly et al. 2013). We flag as intrinsic all systems in this redshift range that show strong absorption in high ions (O VI, Ne VIII, N V, etc.), strong high ions but weak H I, strongly non-Gaussian profiles, or doublet equivalent width ratios close to 1:1 (which may result from partial covering of the source). Similarly, we mask out  $cz_{\text{abs}} < 500 \text{ km s}^{-1}$  as possible high-velocity absorption associated with our Galaxy or absorption from the Local Group<sup>11</sup>. Absorbers in these regions are measured and reported in the tables, but are not included in IGM statistics, nor are these redshift ranges included in the total IGM pathlength calculations.

### 2.4.3. Components and Systems

In the following analyses, we classify IGM absorbers in two ways. First is the self-explanatory *component* analysis where individual fitted velocity components are analyzed as measured. However, it is often more useful to discuss *systems* of components (e.g., Tripp et al. 2008) at nearly the same redshift. Systems are composed of components in the same sight line within a narrow velocity window, which allows lines of different species to be directly related, even if there are small velocity misalignments between them. We adopt this method to manage the ambiguity often present in associating components of one ion with components in another (Figure 2) or even the ambiguity within a given transition composed of multiple, blended components. Detailed analysis of an

<sup>10</sup> An IDL routine to implement the significance level calculation of Keeney et al. (2012) can be found at <http://casa.colorado.edu/~danforth/science/cos/costools.html>.

<sup>11</sup> A subset of COS observations were designed to probe M31, the Magellanic Clouds and Stream, or high-velocity structures in the Milky Way halo. Thus, we exclude the lowest-velocity ( $cz \leq 500 \text{ km s}^{-1}$ ) regions from our IGM survey to limit “double counting” of absorbing structures.

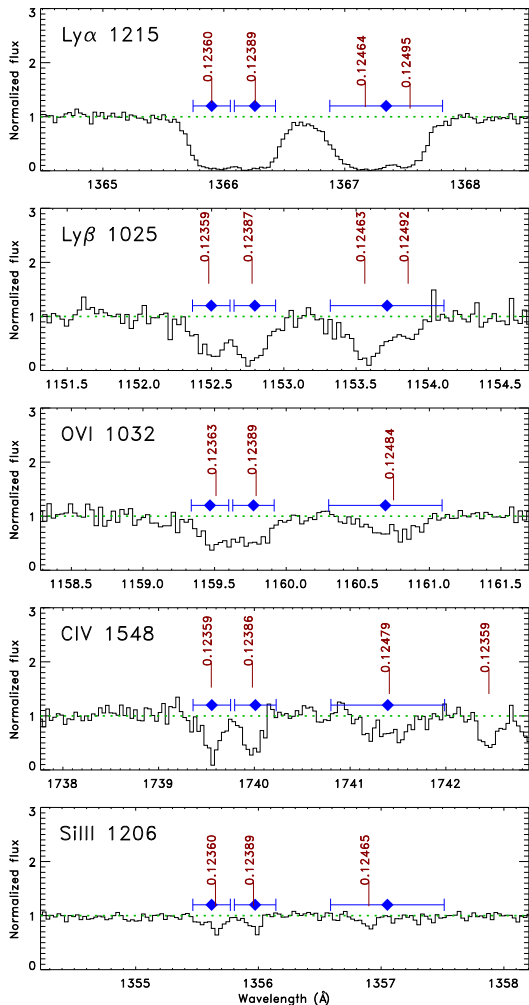


FIG. 2.— Absorption in the PG 1216+069 sight line illustrates the distinction between components and systems. Individual components are denoted with vertical ticks, labeled by redshift, and grouped together into three absorbing systems (blue horizontal bars). Any components that fall within the system velocity range are included in their respective systems. At first glance, the absorbers near  $z \approx 0.1237$  and  $z \approx 0.1247$  appear similar. However, the former complex shows consistent velocity structure in all lines so the components can be unambiguously assigned to one or the other of two narrow ( $\Delta v_{\text{sys}} \approx 40 \text{ km s}^{-1}$ ) systems at  $z = 0.12360$  or  $z = 0.12390$ . The redder system is more ambiguous; while the H I absorption clearly shows two components, the O VI and CIV absorption shows a single, broad component which cannot be unambiguously assigned to either H I component. For this reason, we maintain a single, broader ( $\Delta v_{\text{sys}} = 115 \text{ km s}^{-1}$ ) system at  $z = 0.12474$ .

individual system may reveal more accurate associations (Savage et al. 2014; Stocke et al. 2014), but this depth of analysis is beyond the scope of our large, semi-automated survey. Initially, we defined systems by stepping through the components in a sight line in order of line strength and grouping any other components measured within  $\Delta v_{\text{sys}} = 30 \text{ km s}^{-1}$  into the same system. Systems with stronger, broader lines used  $\Delta v_{\text{sys}} = cW_r/\lambda_0$  to account for ambiguously blended absorption components.

The automatic system-definition algorithm accounted for most strongly-blended absorption components and velocity calibration uncertainties between different wavelength regions in the data. The majority of systems (1888/2611 $\approx$ 72%) were composed of a single line, and

for these there is no distinction between component and system nomenclatures. However, all 723 systems composed of more than a single component, whether multiple, blended components of the same transition or components in multiple transitions, were checked manually. In most cases, the automatic system definitions were confirmed, but the redshifts  $z_{\text{sys}}$  and velocity widths  $\Delta v_{\text{sys}}$  for some systems were adjusted manually to account for obvious, unambiguous component structure. Finally, all measured components were checked to make sure they appear in one, and only one, absorbing system. An example of three systems composed of four components in Ly $\alpha$  is shown in Figure 2.

Systems tend to be broader when more components are included: the 435 two- or three-component systems have a median width close to the nominal minimum  $\Delta v_{\text{sys}} \approx 30 \text{ km s}^{-1}$ . The 240 IGM systems with 4-9 components tend to be broader with  $\Delta v_{\text{sys}} = 36_{-6}^{+26} \text{ km s}^{-1}$ . The 48 richest systems (composed of 10 or more individual components) have a system width of  $\Delta v_{\text{sys}} = 49_{-18}^{+34} \text{ km s}^{-1}$ , and there are only 12 systems with  $100 \text{ km s}^{-1} < \Delta v_{\text{sys}} < 300 \text{ km s}^{-1}$ .

#### 2.4.4. Consistency Checks

The final step in the creation of a line list is to check all line measurements and identifications for consistency. Each line list is screened for features identified as IGM at  $z_{\text{abs}} < 0$  or  $z_{\text{abs}} \gg z_{\text{AGN}}$ . Unidentified lines at  $< 3\sigma$  are rejected. Unidentified  $> 4\sigma$  features are examined and identifications are attempted (though see discussion above regarding unidentified lines). “Orphaned” lines, such as those identified as metal lines or higher-order Lyman lines but without any other detections at the same redshift, are flagged and examined.

We check all multiplet transitions (H I, O VI, N V, Si IV, C IV, Ne VIII, etc.) for consistency in column density. For instance, if a line is identified as O VI 1032 Å at a particular redshift, the 1038 Å O VI transition must appear as a detection of consistent strength, a blend with a stronger feature, or a non-detection consistent with the  $3\sigma$  minimum equivalent width at the expected location in the data. Discrepancies are reevaluated manually.

H I column density and  $b$ -value measurements based on single Lyman line profiles tend to overestimate the line width and underestimate the column density (Danforth et al. 2010a). We determine column density and  $b$ -values for H I via a curve of growth (CoG) fit to multiple Lyman lines. CoG fits are performed for systems at  $z > 0.1$  (where Ly $\beta$  is covered in COS data) with  $N_{\text{HI}} > 10^{14} \text{ cm}^{-2}$  in any individual Lyman line. Any outlying single-line measurements or poor CoG solutions are reevaluated manually. In most cases, the CoG H I solution is more accurate than a single-line Ly $\alpha$  measurement. However, while the CoG solution to a system with multiple velocity components tends to preserve total column density in the lines, the  $b$ -value may be artificially broad. We do not attempt CoG solutions to metal-ion lines because most of their absorption lines are not heavily saturated. Neither is there enough  $f\lambda$  contrast between transitions for a well-constrained CoG solution.

#### 2.5. Biases and Systematics

There should be little bias in the IGM sample due to the choice of AGN in this study. The sight lines were chosen from a large archive of *HST*/COS observing programs reflecting a broad range of scientific objectives. The one unifying characteristic of the sight lines is that they are toward UV-bright targets. Outside a relatively small proximity zone, where the AGN may have undue effect on the local photoionization, the source luminosity has no bearing on the properties of the IGM sample. It can be argued that using UV-bright sources selects against strong H I absorption at any redshift along the line of sight; Lyman Limit systems with  $\log N_{\text{HI}} \geq 17.2$  are opaque ( $\tau_0 > 1$ ) to Lyman continuum photons at  $\lambda < (1 + z_{\text{abs}}) \times 912 \text{ \AA}$ , but this is only true for  $z_{\text{abs}} \gtrsim 0.4$  where the Lyman continuum redshifts sufficient to block a substantial part of the FUV band. Lyman Limit systems at  $z < 1$  are rare ( $dN/dz \approx 0.33$ ; Stevans et al. 2014; Ribaud et al. 2011), but our sample includes one such case (SBS 1108+560,  $z_{\text{LLS}} = 0.4632$ ). Generally the redshifted Lyman continuum flux is only moderately absorbed (Shull, Stevans, & Danforth 2012; Stevans et al. 2014), even in the rare, strong H I systems at higher  $z$ . Most of our AGN are at  $z_{\text{em}} < 0.4$  where LLSs make no difference to the observed spectrum in the Ly $\alpha$  forest.

There is a small bias in that fifteen of the 82 sight lines were originally proposed because they probe specific galaxies near the AGN sight line. Measured covering factor of Ly $\alpha$  absorbers with  $N > 10^{13} \text{ cm}^{-2}$  at  $R < R_{\text{vir}}$  are  $\sim 80\%$  for  $L > L^*$  and  $0.1 - L^*$  galaxies (Stocke et al. 2013). Prochaska et al. (2011) finds even higher covering factors for  $0.1 - 1L^*$  galaxies, statistically consistent with 100%. Tumlinson et al. (2011) find similarly high covering factors for O VI around  $L > L^*$  star-forming galaxies. While Stocke et al. 2013 find that dwarfs have smaller covering factors ( $\sim 50\%$  at  $R < R_{\text{vir}}$ ) it turns out that that sample was heavily biased by Virgo Cluster sightlines. Bordoloi (private communication) finds very high covering factors ( $> 80\%$ ) for Ly $\alpha$  at  $R < R_{\text{vir}}$  in his COS dwarfs sample. Given the observed high covering factor of Ly $\alpha$  absorption detected within  $\pm 400 \text{ km s}^{-1}$  of a galaxy velocity, this implies that  $\sim 15$  metal-line absorbers are present in our overall sample due to this selection bias.

Column densities inferred from single, saturated absorption lines can underestimate the true column density as determined via a more robust curves of growth, sometimes dramatically (e.g., the  $cz = 1590 \text{ km s}^{-1}$  H I absorber toward 3C 273 first measured by Weymann et al. (1995) based on a single Ly $\alpha$  absorber, subsequently corrected with a multi-line curve-of-growth by Sembach et al. (2001). For the vast majority of H I Lyman lines, COS absorption line profiles are well-resolved and our Voigt profile fits should give accurate single-line column density measurements even in the case of moderate saturation in the line core ( $\tau_0 = 1 - 3$ ). However, stronger Lyman lines should be conservatively treated as lower limits on the column density. A line-center optical depth  $\tau_0 = 3$  corresponds to a transmitted flux of 5%. Given the typical S/N of 20 in the sample, we feel this is a conservative limit on where single-line column densities can be trusted. Of the 5121 IGM absorption lines in the catalog, 579 (11%) show  $\tau_0 \geq 3$  (Figure 3). Subdividing by transition, 12% of Ly $\alpha$  absorbers

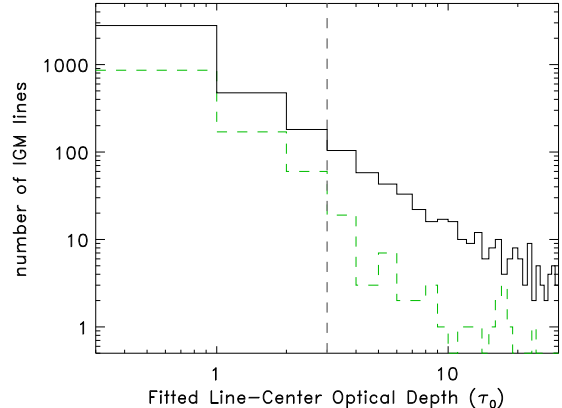


FIG. 3.— Histogram of fitted line-center optical depth ( $\tau_0$ ) for 3966 H I Lyman lines (black solid) and 1155 metal-ion lines (green dashed) identified as IGM absorption. Given the typical quality of the COS spectra ( $S/N \gtrsim 20$ ), column density measurements of mildly-saturated lines ( $\tau_0 \lesssim 3$ ) should be accurate. However,  $\sim 13\%$  of Lyman lines are saturated  $\tau_0 > 3$ , so column density measurements of these single lines should be taken as lower limits. Saturated metal lines are much less common:  $\sim 5\%$ .

are saturated at  $\tau_0 \geq 3$  as are 15% of higher-order Lyman lines. Saturated metal-line absorbers are rare, comprising only 5% of the total sample. These are also listed as lower limits in the line lists.

Most of our analysis in the remainder of the paper is based on system-level measurements where  $N_{\text{HI}}$  is determined via a robust curve of growth for stronger absorbers. Lower limits on column density of individual lines should not be an issue. However, we list the individual column density measurements as lower limits in the line catalog. There are 118 Ly $\alpha$  absorbers at low-redshift ( $z < 0.1$ ) where Ly $\beta$  is not available for a CoG measurement. These systems are among those excluded from the uniform sample discussed in Section 2.5.

Some science programs were designed to probe individual extragalactic objects or near-field structures (the Magellanic Stream, M31). This presents a bias for a few specific absorbers but the population of absorbers along the sight line as a whole is unbiased. In a few other cases, adjacent sight lines may be sampling the same structures in absorption, creating a “double-counting” bias. The closest pair of sight lines in this survey is separated by  $9.3'$  and three other pairs are separated by less than a degree on the sky. The redshift range over which the sight lines are separated by less than 1 Mpc (where correlated absorption may be expected) is only  $\Delta z \approx 0.1$  or  $\sim 0.5\%$  of the total survey pathlength. The overall bias on the IGM absorber catalog from sight line selection is very small.

Most of the absorbers in the catalog are relatively narrow features ( $b < 50 \text{ km s}^{-1}$ ). The median doppler width and  $\pm 1\sigma$  range for IGM components are  $b = 33_{-14}^{+17} \text{ km s}^{-1}$ . Automated line-finding codes search for lines at  $b = 20, 50, \text{ and } 100 \text{ km s}^{-1}$ , and profile-fitting codes fit features with a parameter range  $5 < b < 150 \text{ km s}^{-1}$ . However, COS is optimized for the detection of narrow lines, and there is an inherent bias in this catalog toward lines close to the resolution limit. We define a sensitivity as a function of  $b$ -value,  $S(b) \equiv [W_{\text{min}}(b)/W_{\text{min}}(b =$

10)]<sup>-1</sup> where  $W_{\min}(b)$  is the minimum equivalent width for a line of a Doppler parameter  $b$  in data of a given  $S/N$ . There is a slight dependence of  $S(b)$  on observed wavelength, but it is insensitive to  $S/N$ . For  $b = 30 \text{ km s}^{-1}$ , we see  $S(30) = 0.66$ ; COS data are only 2/3 as sensitive to  $30 \text{ km s}^{-1}$  lines as they are to those near the resolution limit of the data ( $b \sim 10 \text{ km s}^{-1}$ ). The sensitivity gets worse for broader lines:  $S(50) = 0.5$ ,  $S(100) = 0.35$ , and  $S(200) = 0.23$ . Thus, there is a bias against weak, broad lines in the data, even with accurate knowledge of the AGN continuum and binning appropriate to the line width. In addition, the continuum fitting routine uses bins of 5-15 Å in width, so features broader than several Angstroms ( $b \gtrsim 300 \text{ km s}^{-1}$ ), whether they be actual absorption lines, AGN emission lines, flux calibration uncertainties, or other instrumental features, tend to be fitted as part of the continuum.

The two medium-resolution COS/FUV gratings cover the Ly $\alpha$  forest for absorbers out to  $z \approx 0.47$ . For weak absorbers, column density can be determined from measurements of the Ly $\alpha$  line alone with reasonable accuracy. However, H I column density measurements based on saturated Ly $\alpha$  lines alone tend to underpredict the true column density (Shull et al. 2000; Sembach et al. 2001; Wakker et al. 2015). CoG fits to multiple H I transitions tend to give a more realistic  $N_{\text{HI}}$  value for  $N_{\text{HI}} \gtrsim 10^{14} \text{ cm}^{-2}$ . In a typical COS/FUV dataset, the Ly $\beta$  transition redshifts into the G130M detector at  $z \approx 0.1$ . In order to limit column density uncertainty between stronger H I systems at low redshift (measured from Ly $\alpha$  alone) and higher redshift (where multi-line CoG solutions are used), we define a *uniform*, redshift-limited subsample of IGM systems: weak H I systems ( $\log N_{\text{HI}} < 13.5$ ) are included regardless of redshift, but stronger absorbers ( $\log N_{\text{HI}} \geq 13.5$ ) are included only at  $z_{\text{abs}} \geq 0.1$  where a more accurate, multi-line CoG solution is possible; either Ly $\alpha$ +Ly $\beta$  or Ly $\beta$ +Ly $\gamma$  at minimum. The limited sample (2256 systems) is only slightly smaller than the full COS sample (2577 systems) since only the stronger systems at low redshift are excluded. However, this limited sample provides a more uniform analysis of the distribution of H I absorbers in the low-redshift IGM.

Given the huge number of IGM absorber systems (>2600) and the substantial pathlength ( $\Delta z > 20$ ) used for their discovery, the sample variance should be small and adds negligible uncertainty to the Poisson errors. However, based on a previous jack-knife style resampling exercise done for a smaller sample (Penton, Stocke, & Shull 2004), we estimate that cosmic variance can add significant uncertainty to our sample at  $\log N_{\text{HI}} \geq 15$  (i.e., sub-sample sizes with  $\mathcal{N} \lesssim 100$  absorbers). For order of magnitude sized bins starting at  $\log N_{\text{HI}} = 15, 16,$  and  $17$ , we estimate that cosmic variance adds (in quadrature) 17%, 33% and 86% to the Poisson errors in those bins. Since metal-line systems are almost always attached to H I systems, the cosmic variance in those samples is small despite their small numbers.

### 3. THE CATALOG

To facilitate further analysis, and as a service to the community, we present data products as a High-

Level Science Product (HLSP) in a partnership with the Mikulski Archive for Space Telescope (MAST) at <http://archive.stsci.edu/prepds/igm/>. The following products are included for each of the 82 AGN sight lines in this survey:

- A fully-reduced, coadded spectrum in heliocentric wavelength coordinates as discussed in Section 2 in FITS format including wavelength, flux, error, and local exposure time vectors. Also included are the “line-less” error, continuum fit, continuum fit uncertainty, and a flag for pixels used in the continuum fit.
- A full list of all absorption features measured at  $SL > 3$  sorted by observed wavelength in ASCII format. Each line list table includes line wavelength, significance level (as described in Section 2.4), line identity, redshift of the feature, equivalent width and  $1\sigma$  equivalent width uncertainty. Extragalactic lines additionally have listed Doppler  $b$ -values and measured  $\log N$  values, both with uncertainties, and the reduced  $\chi^2$  value of the line fit. Three final columns are used to flag likely Galactic (ISM) lines, likely AGN intrinsic lines, and the approximate line-center optical depth  $\tau_0$ .
- A table in ASCII format of extragalactic absorption lines grouped by system redshift as described in Section 2.4. Only extragalactic absorbing systems at  $z > 0$  are listed. The first two columns identify each system by system redshift,  $z_{\text{sys}}$ , and velocity half-width,  $\Delta v_{\text{sys}}$  followed by the same columns of measured quantities in the line lists and counts of the number of total lines which comprise the system and the number of metal lines.
- A multi-page “atlas” showing the reduced data, continuum fit, and identified lines. The first panel of the atlas shows an overview of the entire spectrum in context with some observational details from Tables 1 and 2 above. Subsequent panels show the entire range of COS data in 25Å segments with identified absorption features marked with vertical ticks and labeled where possible. Red ticks and labels denote  $z > 0$  features with abbreviated line-ID and redshift. Green ticks show  $v \approx 0$  ISM features. A sample page of the seven-page atlas for 3C 57 is shown in Figure 4.

In addition to the individual sight lines, we provide the median-combined Galactic foreground spectrum, both in FITS format and as a multi-page atlas in the same format as the individual sight line atlases. A portion of this spectrum is shown in Figure 1.

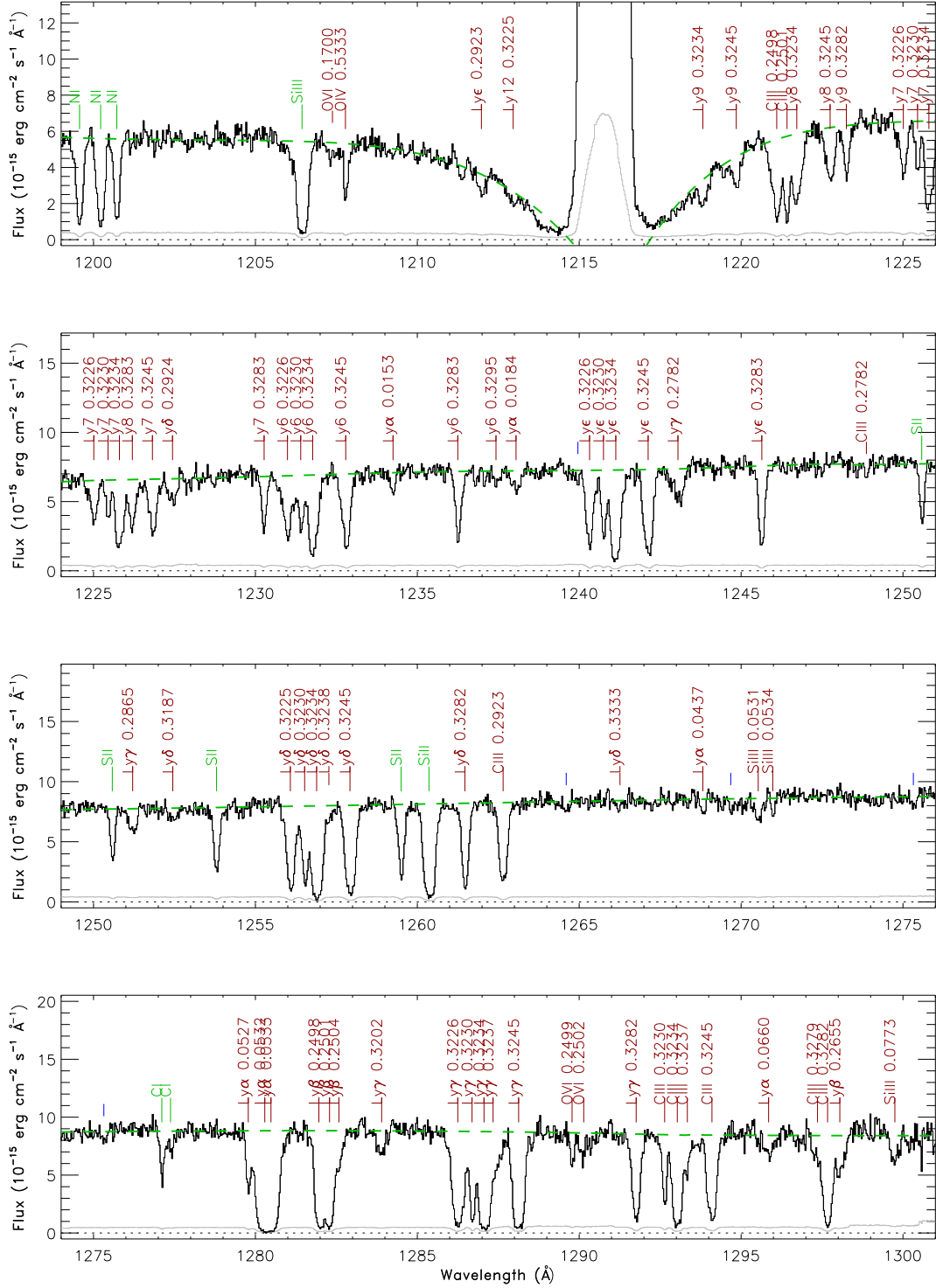


FIG. 4.— Sample atlas page for 3C57. Coadded flux and error vectors are shown in black and grey, respectively. Green dashed line shows the continuum. Each page covers 100 Å of the COS spectrum. Red text and ticks denote IGM absorbers (identified by species and redshift). Green ticks show  $v \approx 0$  ISM features. Blue ticks mark lines with no identification.

### 3.1. Erratum

We note that a previous version of the HLSP was released in early 2014. While similar in content to this 2016 catalog, this version was based on an earlier data reduction pipeline. A number of instrumental artifacts were included as bone-fide IGM absorption lines. In the intervening period, our data reduction pipeline was improved tremendously. The current version of the HLSP should be largely free of instrumental features. Also, the signal-to-noise of the coadded data has been improved by  $\sim 10\%$  in most cases due to better coaddition techniques. Data from the 2014 IGM catalog should be discarded in favor of the current version.

## 4. RESULTS

We measure 5138 significant IGM absorption components which comprise 2611 distinct absorbing systems along 82 sight lines over total H I redshift pathlength  $\Delta z = 21.7$ . This is the largest catalog of low- $z$  IGM absorption to date and represents three times more sight lines and absorbers than any previous low-redshift IGM absorber study (Lehner et al. 2007; Danforth & Shull 2008; Tripp et al. 2008; Tilton et al. 2012) with greatly-improved sensitivity to weaker absorbers ( $\Delta z \approx 18$  for  $N_{\text{HI}} \approx 10^{13} \text{ cm}^{-2}$ ). The catalog is intended to be useful in many areas of astrophysics, and many follow-on studies are planned on specific, more focused areas of research (e.g., Shull, Danforth & Tilton 2014, on the IGM metal evolution). Here, we present some global results from the catalog. Unless otherwise noted, all statistics refer to IGM *systems*, not individual components.

### 4.1. H I Absorber Distribution

The normalized frequency of absorbing systems  $dN/dz$  and the bivariate distribution of H I absorbers as a function of column density and redshift,  $\partial^2 \mathcal{N} / \partial N \partial z$ , are important quantities in low- $z$  cosmology. Line density is an important probe of cosmic structure in the linear regime and, in comparison with simulations, yields constraints on density, the spectral energy distribution and intensity of the ionizing background (Kollmeier et al. 2014; Shull et al. 2015), the evolution of structures, thermal structures, and the processes of galaxy feedback (e.g., Davé & Tripp 2001; Cen & Fang 2006; Davé et al. 2010; Smith et al. 2011; Shull, Smith, & Danforth 2012; Kollmeier et al. 2014; Shull et al. 2015).

Calculating  $dN/dz$  accurately requires both good counting statistics and knowledge of the pathlength  $\Delta z(N)$  covered in the survey for absorbers of a given column density  $N$ . Since sensitivity is neither a constant between sightlines nor in different spectral ranges, we must correct for incompleteness in the weak absorbers by calculating the effective redshift pathlength,  $\Delta z(N_{\text{min}})$ , sensitive to minimum column density,  $N_{\text{min}}$ . The effective absorption redshift pathlength  $\Delta z(N)$  is calculated in a manner similar to that used in DS08, and we refer the reader there for details. Briefly, we calculate the  $3\sigma$  minimum equivalent width,  $W_{\text{min}}(\lambda)$ , as a function of wavelength in each spectrum ( $4\sigma$  for Ly $\alpha$  detections as discussed above). We use the Galactic foreground COS template described above to mask portions of the spectrum with strong Galactic ISM regions. The  $W_{\text{min}}(\lambda)$  vector is then translated into  $N_{\text{min}}(z)$  for each ion. Since

many species have line multiplets, the minimum column density  $N_{\text{min}}(z)$  is different for different transitions of the same species. For instance, the O VI 1038 Å transition is only half as sensitive to absorption as the stronger O VI 1032 Å line. At  $z_{\text{abs}} = 0.178 \pm 0.003$  the stronger transition lies within the strong absorption from the Galactic DLA at 1213-1218 Å where we have no sensitivity, but the weaker O VI line lies in clear continuum at 1223 Å. Thus, we can still detect O VI absorption at that redshift, albeit at half the usual sensitivity. As in the line lists, the pathlength at  $(cz_{\text{AGN}} - cz_{\text{abs}})/(1 + z_{\text{AGN}}) \leq 1500 \text{ km s}^{-1}$  and  $cz_{\text{abs}} < 500 \text{ km s}^{-1}$  is excluded to limit AGN-intrinsic and Local Group absorbers, respectively. In cases where probable intrinsic absorbers are seen at  $cz_{\text{abs}}/(1 + z_{\text{AGN}}) > 1500 \text{ km s}^{-1}$  with respect to the AGN, that limit is used instead.

TABLE 4  
ABSORPTION PATHLENGTHS  $\Delta z$  AND COMPLETENESS LIMITS

Species	Maximum		$z_{\text{abs}}$ range	log $N$ completeness		
	$\Delta z$	$\Delta X^a$		75%	50%	25%
H I	21.74	35.92	$< 0.75^b$	13.09	12.93	12.77
H I <sup>c</sup>	19.23	...	$< 0.75^c$	13.04	12.89	12.73
O VI	14.49	27.73	0.1 – 0.73	13.56	13.42	13.28
N V	19.33	28.09	$< 0.45$	13.31	13.18	13.03
C IV	8.85	10.33	$< 0.16$	13.26	13.12	12.96
Si IV	14.60	18.96	$< 0.28$	12.81	12.64	12.48
Si III	20.03	29.83	$< 0.49$	12.33	12.20	12.04
C III	10.40	22.61	0.16 – 0.8	12.84	12.70	12.56
Ne VIII	2.32	7.54	0.47 – 0.85	14.08	13.88	13.70

<sup>a</sup> Co-evolving absorber pathlength (Eq. 2).

<sup>b</sup> In principle, the Lyman continuum redshifts out of the COS/G160M detector at  $z = 0.97$ . However, in practice, H I is most reliably identified and measured using Ly $\alpha$  or Ly $\beta$  which limits the effective range to  $z < 0.75$ .

<sup>c</sup>  $z$ -limited, uniform sample described in Section 2.5.

Detection limits as a function of redshift are assembled for each species (H I, O VI, C IV, etc.) in each sight line, and the accumulated pathlengths at various limiting column densities and redshift ranges are totalled. For strong H I absorbers at any redshift, the total pathlength  $\Delta z_{\text{HI}} = 21.74$ , but the survey completeness has dropped to  $\leq 50\%$  at  $\log N_{\text{HI}} \leq 12.93$ . The detailed effective redshift path  $\Delta z(N)$  is used to correct for completeness in our counting statistics to calculate  $dN/dz$ . Maximum pathlengths in redshift  $\Delta z$  and co-evolving absorber pathlength  $\Delta X$  (Bahcall & Peebles 1969) are related by

$$\Delta X = \int_{z_1}^{z_2} \frac{(1+z)^2}{[\Omega_m(1+z)^3 + \Omega_\Lambda]^{1/2}} dz, \quad (2)$$

and listed in Table 4 for H I and seven metal species. The fourth column shows the approximate redshift range over which an ion can be effectively identified in COS/FUV data. The final three columns show the column densities at which the IGM survey is 75%, 50%, and 25% complete.

Figure 5 shows the distribution of total H I systems as a function of column density, together with the effective path length  $\Delta z(N_{\text{HI}})$  and the differential distribution ( $\partial^2 \mathcal{N} / \partial \log N \partial z$ ) after it is corrected for completeness. Figure 6 shows the same distribution for

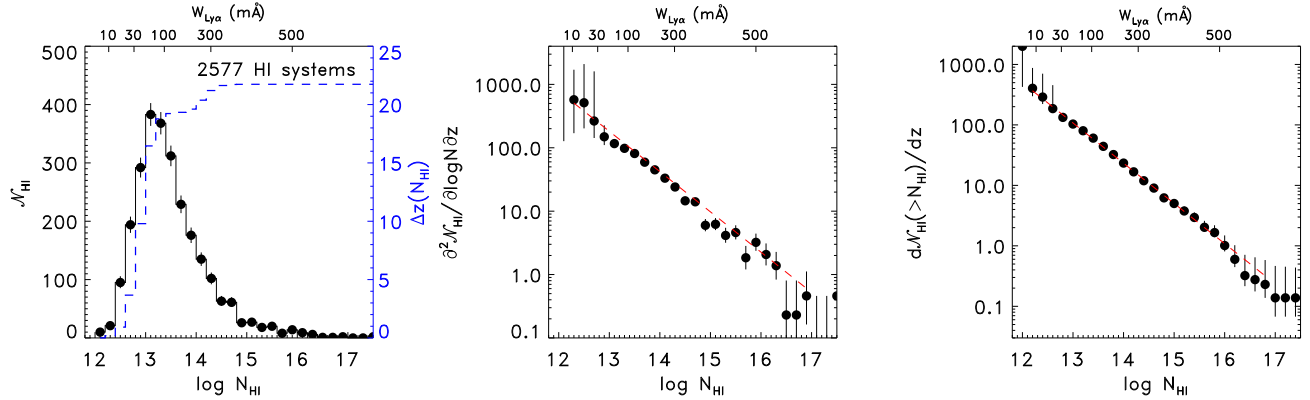


FIG. 5.— HI detection statistics for the full ( $0 \leq z_{\text{abs}} < 0.75$ ) sample of 2577 IGM HI systems. Left panel shows the number of systems  $\mathcal{N}$  per 0.2 dex column density bin. Error bars are one-sided Poisson uncertainty corresponding to  $\pm 1\sigma$ . The dashed curve and right-hand axis show the effective pathlength  $\Delta z$  as a function of column density. The differential absorber frequency  $\partial^2 \mathcal{N}(N)/\partial \log N \partial z$  (Eq. 2) is shown in the middle panel. The right panel shows the integrated system frequency  $d\mathcal{N}(> N)/dz$ . Power law fits to the differential and cumulative distributions are shown as dashed lines. Equivalent width values for  $b = 25 \text{ km s}^{-1}$  Ly $\alpha$  lines are shown on the top axis of each panel.

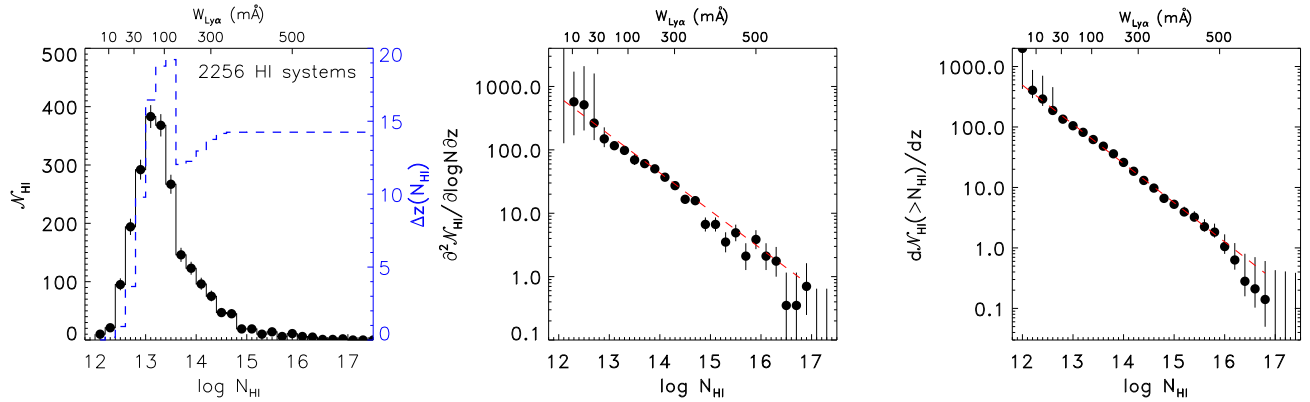


FIG. 6.— Same as Fig. 5 but for the “uniform” sample (2256 IGM HI systems); weak systems at all redshifts are used, but stronger systems ( $\log N \geq 13.5$ ) are only included at  $z_{\text{abs}} \geq 0.1$  where multi-line CoG solutions are available.

the more uniform  $z$ -limited sample as described in Section 2.5. Summing over column density down to a given  $N_{\text{HI}}$ , we find the cumulative absorption system frequency  $d\mathcal{N}(> N)/dz$ , which can be fitted with a power law of the form

$$\frac{d\mathcal{N}(> N)}{dz} = C_{14} \left( \frac{N}{10^{14} \text{ cm}^{-2}} \right)^{-(\beta-1)}. \quad (3)$$

Here, we use the traditional notation of  $\beta$  as the index to the *differential* distribution  $d^2 \mathcal{N}/dN dz \propto N^{-\beta}$ ; the slopes of the cumulative and differential distributions differ by one. Fitting the differential distribution of the uniform  $z$ -limited sample of 2256 absorbers, we find  $\beta = 1.65 \pm 0.02$  for systems in the range  $12 \leq \log N \leq 17$  with a normalization constant  $C_{14} = 25 \pm 1$  at the fiducial column density of  $N_{\text{HI}} = 10^{14} \text{ cm}^{-2}$  (corresponding to  $W_{\text{r}} \approx 240 \text{ m\AA}$  for  $b = 25 \text{ km s}^{-1}$ ). The full sample of 2577 systems has fit parameters  $\beta = 1.67 \pm 0.01$  and  $C_{14} = 23 \pm 1$ . For ease of comparison with other observations and with simulation results, we list column density bins, number of absorption systems per bin, redshift pathlength, and  $\partial^2 \mathcal{N}/\partial N \partial z$  values for the uniform HI subsample in Table 5.

In previous surveys (e.g., Danforth & Shull 2005, 2008), we adopted  $\beta = 2$  as the critical index separating “top-heavy” and “bottom-heavy” scenarios, with total IGM mass dominated by the few high-column density systems or the many lower-column density systems. However, this assumption is simplistic as it ignores the dependence on column density of the ionization fraction (and metallicity in the case of metal ion absorbers). These issues are discussed in detail in Shull, Smith, & Danforth (2012) who used simulations to derive the  $N$ -dependence of thermal phases and metallicities in the IGM.

The sample quantities in the COS HI systems are similar to those found in previous low- $z$  IGM surveys using smaller samples; Tilton et al. (2012) found  $\beta_{\text{HI}} = 1.68 \pm 0.03$  in a sample of 746 absorbers over pathlength  $\Delta z_{\text{HI}} = 5.38$ . Slopes of  $\beta_{\text{HI}} = 1.65 \pm 0.07$ ,  $1.76 \pm 0.06$ , and  $1.73 \pm 0.04$  were found in smaller Ly $\alpha$ /HI surveys by Penton, Stocke, & Shull (2004), Lehner et al. (2007), and DS08, respectively. Numerical simulations also agree, e.g.,  $\beta_{\text{HI}} = 1.70$  at  $z = 0$  from Davé et al. (2010).

It has been suggested (Rudie et al. 2013) that a small break in the power law nature of  $d\mathcal{N}/dz$  may exist for

IGM absorbers at  $z \approx 2 - 3$  corresponding to the association of strong absorbers with galaxy halos and weaker absorbers with unvirialized intergalactic matter. We searched for a fit to a broken power law to the cumulative  $dN/dz$  in the uniform H I sample with both slopes and the column density of the breakpoint as free parameters. No significant break is found in our low- $z$  sample.

TABLE 5  
HI AND O VI  $\partial^2 \mathcal{N}(N)/\partial \log N \partial z$  VALUES

$\log N$	$N_{\text{HI}}$	$\Delta z_{\text{HI}}$	$\frac{\partial^2 \mathcal{N}(N_{\text{HI}})}{\partial \log N \partial z}$	$N_{\text{OVI}}$	$\Delta z_{\text{OVI}}$	$\frac{\partial^2 \mathcal{N}(N_{\text{OVI}})}{\partial \log N \partial z}$
12.2-12.4	21	0.18	$570^{+1000}_{-400}$	...	...	...
12.4-12.6	95	0.93	$510^{+1000}_{-310}$	...	...	...
12.6-12.8	194	3.67	$260^{+1000}_{-120}$	...	...	...
12.8-13.0	292	9.79	$150^{+80}_{-40}$	2	0.24	$42^{+150}_{-37}$
13.0-13.2	383	16.46	$120 \pm 10$	6	0.91	$33^{+78}_{-25}$
13.2-13.4	368	18.78	$98 \pm 5$	17	4.13	$21^{+9}_{-33}$
13.4-13.6	267	19.23	$69^{+17}_{-12}$	40	9.16	$22^{+7}_{-5}$
13.6-13.8	146	12.03	$61 \pm 5$	62	12.65	$25^{+4}_{-3}$
13.8-14.0	123	12.25	$50 \pm 5$	69	13.81	$25 \pm 3$
14.0-14.2	96	12.96	$37 \pm 4$	47	14.13	$17^{+3}_{-2}$
14.2-14.4	75	13.75	$27^{+4}_{-3}$	24	14.36	$8.4^{+2.1}_{-1.7}$
14.4-14.6	47	14.17	$17^{+3}_{-2}$	10	14.43	$3.5^{+1.5}_{-1.1}$
14.6-14.8	45	14.24	$16^{+3}_{-2}$	2	14.46	$0.69^{+0.91}_{-0.45}$
14.8-15.0	19	14.25	$6.7^{+1.9}_{-1.5}$	1	14.48	$0.35^{+0.79}_{-0.29}$
15.0-15.2	19	14.25	$6.7^{+1.9}_{-1.5}$	...	...	...
15.2-15.4	10	14.25	$3.5^{+1.5}_{-1.1}$	...	...	...
15.4-15.6	14	14.25	$4.9^{+1.7}_{-1.3}$	...	...	...
15.6-15.8	6	14.25	$2.1^{+1.3}_{-0.8}$	...	...	...
15.8-16.0	12	14.25	$4.2^{+1.6}_{-1.2}$	...	...	...
16.0-16.2	6	14.25	$2.1^{+1.3}_{-0.8}$	...	...	...
16.2-16.4	4	14.25	$1.4^{+1.1}_{-0.7}$	...	...	...
16.4-16.6	0	14.25	$0.0^{+0.65}_{-0.00}$	...	...	...
16.6-16.8	1	14.25	$0.35^{+0.81}_{-0.29}$	...	...	...
16.8-17.0	2	14.25	$0.70^{+0.93}_{-0.45}$	...	...	...
17.0-17.2	1	14.25	$0.35^{+0.81}_{-0.29}$	...	...	...

#### 4.1.1. Line-Width Distribution

Measuring the Doppler  $b$  parameter of an absorption system is more prone to error than measuring the column density due to several systematic effects. The profile-fitting routines used here take into account the instrumental line spread function (Kriss 2011), but the fitted  $b$  is still the quadratic sum of thermal and non-thermal line widths. Unresolved component structure and noise in the line profile can both affect the measured  $b$  value of a system. Profiles fitted to Ly $\alpha$  components are known to systematically over-estimate the  $b$  value (Danforth et al. 2010a) so single-transition  $b$  measurements should be used with caution. Curve-of-growth fits can provide a more accurate measurement of  $b_{\text{HI}}$  in absorbers with a simple velocity structure, but it is likely that most strong H I absorbers contain multiple, unresolved velocity components.

We limit these effects by examining the  $b$ -value distribution of only those H I systems fitted with a single velocity component. Figure 7 shows that the distribution of  $b$  values for weak, single-component systems ( $N_{\text{HI}} \leq 10^{13.5} \text{ cm}^{-2}$ ) has a median  $b$ -value of  $29.6 \pm 0.5$

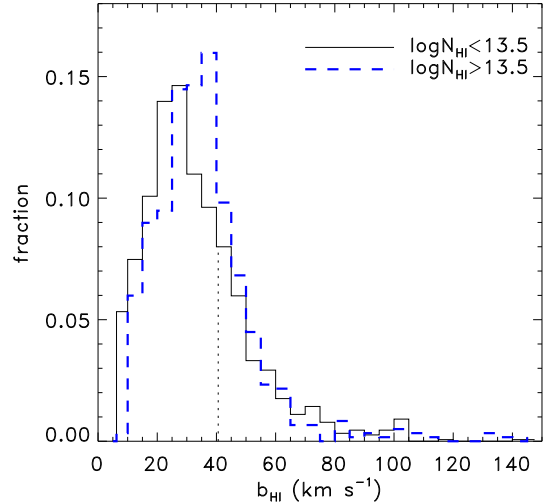


FIG. 7.— Distribution of line widths for H I systems in the uniform sample. To limit broadening introduced by multiple components, we analyze H I lines fitted with only a single resolved velocity component. The weak ( $\log N \leq 13.5$ ) and strong ( $\log N > 13.5$ ) samples show median  $b$ -values of  $29.6 \text{ km s}^{-1}$  and  $33.8 \text{ km s}^{-1}$ , respectively. The dotted line marks  $b = 40.6 \text{ km s}^{-1}$ , the line width corresponding to pure thermal broadening at  $T = 10^5 \text{ K}$ . The FWHM is  $1.67b$ .

$\text{km s}^{-1}$  and a  $\pm 1\sigma$  range of  $17 - 48 \text{ km s}^{-1}$ . Stronger single-component systems ( $N_{\text{HI}} > 10^{13.5} \text{ cm}^{-2}$ ) have a larger median ( $b = 33.8 \pm 0.5 \text{ km s}^{-1}$ ) though a similar range ( $20 - 49 \text{ km s}^{-1}$ ). The difference in distributions suggests that stronger absorbers may include unresolved velocity components, artificially increasing the line width. However, it may not be significant since, in the uniform sample, strong H I systems are analyzed through a multi-transition CoG while the weak systems are measured via a single Ly $\alpha$  component.

Both strong and weak H I line-width distributions have a long tail toward broader widths. Since the width of a line is a product of both thermal and non-thermal contributions, the measured  $b$  parameter of an absorption line can set an upper limit on the temperature of the gas. For Ly $\alpha$  components,  $T = 10^5 \text{ K}$  corresponds to  $b = 40.6 \text{ km s}^{-1}$  if all broadening is thermal in nature. These broad Ly $\alpha$  absorbers (BLAs) can provide a tracer of WHIM gas independent of metallicity. The weak and strong samples in Figure 7 show BLA fractions of  $\sim 26\%$  and  $\sim 28\%$ , respectively. However, we caution that unresolved velocity components can contribute non-thermal broadening to a line profile, so the BLA fractions quoted above are more realistically upper limits to their true values. For more discussion, see Richter et al. (2006); Lehner et al. (2007); Danforth et al. (2010a); Savage et al. (2010, 2014). In a more intensive evaluation of 85 O VI components from this sample by Savage et al. (2014), 45 of which have well-aligned H I Ly $\alpha$  components, only 14 components have H I and O VI line widths indicative of  $T > 10^5 \text{ K}$  gas. Therefore, the fraction of BLAs which unambiguously trace WHIM gas is a small fraction of the total H I+O VI absorber population.

#### 4.2. Metal Absorbers

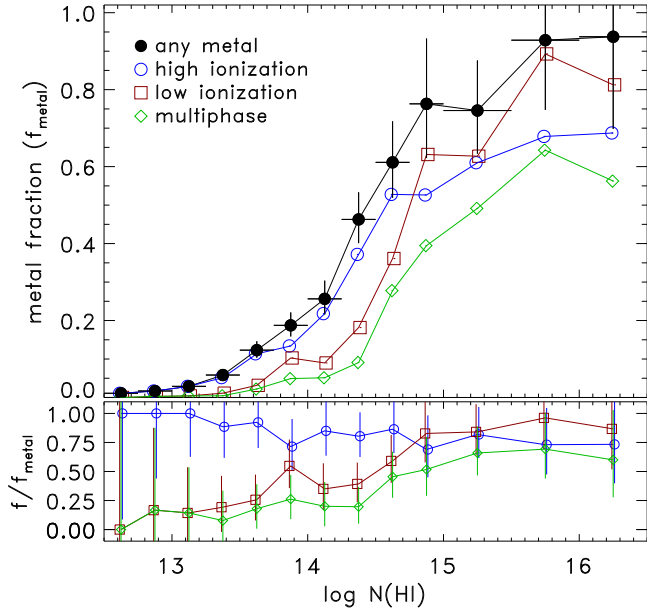


FIG. 8.— Fraction of IGM HI absorbers in which metal ions are also detected as a function of HI column density. Black points (filled circles) show the fraction of IGM systems with a detection in any metal species, while blue (open circles) and red (open squares) show the fraction with detections in highly-ionized metals (O VI, N V, C IV, Ne VIII) and low-ionization metals (Si II/III/IV, C II/III), respectively. Green diamonds show the fraction of multiphase systems, i.e., systems with both high- and low-ionization detections. The bottom panel shows the relative fraction of high- and low-ionization detections as a function of detections in any metal ion.

The majority of extragalactic absorption components are Lyman-series lines of H I ( $4234/5138 \approx 82\%$ ), and the majority of those ( $2946/4234 \approx 70\%$ ) are Ly $\alpha$ . Metals are detected in 418 IGM systems or  $\sim 15\%$  of all IGM systems. This fraction is strongly dependent on H I column density (Figure 8). For weak H I systems with  $12.5 \leq \log N_{\text{HI}} \leq 13.5$ , metals appear in only 48/1465 ( $\sim 3\%$ ). For systems  $13.5 \leq \log N_{\text{HI}} < 14.5$ , the metal fraction rises to 177/818 ( $\sim 22\%$ ). For the strongest IGM systems ( $\log N_{\text{HI}} \geq 14.5$ ), metals are nearly ubiquitous ( $157/212 \approx 74\%$ ). Two effects probably combine to produce the steeply rising metal fraction seen in Figure 8. First is the finite sensitivity of COS spectra to weak absorbers; metal lines in the IGM tend to be weaker than their corresponding Ly $\alpha$  absorbers and thus may not be above the detection limit for weak H I lines. Second, weak absorbers are often associated with the diffuse IGM far from galaxies where metallicity is likely to be very low, while strong absorbers are often associated with higher-metallicity galaxy halos. The 50% “cross-over” point for metal-bearing absorbers is  $\log N_{\text{HI}} \approx 14.5$ , the same column density where  $\sim 50\%$  of absorbers are found within one virial radius of a galaxy (Stocke et al. 2014).

If we subdivide the metal systems into highly-ionized species (O VI, N V, C IV) and low-ionization species (Si II/III/IV, C II/III), we see that systems with high-ionized metals are relatively more common than low-ionization metals at  $\log N_{\text{HI}} < 14$ , while they become comparable in stronger H I systems (Figure 8, bottom panel). This is easily explained by recognizing that H I

is, itself, a low-ionization species. Systems in which O VI and other highly-ionized metals can exist will have a lower neutral fraction and thus lower  $N_{\text{HI}}$  for a given total column density.

The most common metal detection is in one or both lines of the O VI doublet ( $1031.93, 1037.64 \text{ \AA}$ ) which appear in 280 IGM systems. Lithium-like doublet transitions of C IV (70 systems) and N V (59 systems) are also common. Absorption in the strong, singlet lines of Si III ( $\lambda 1206$ , 123 systems) and C III ( $\lambda 977$ , 115 systems) and doublet Si IV ( $\lambda \lambda 1393, 1402$ ; 45 systems) trace moderately-ionized IGM. In addition, transitions of twenty other metal ions are observed in very small numbers; the total census of metal-ion species seen in IGM absorbers is O I/II/III/IV/VI, N II/III/IV/V, C II/III/IV, Si II/III/IV, S IV/V/VI, Fe II, Ne VIII, P II, and Al II. We discuss the statistics of the more common metal-ions below. A comparison of these with higher-redshift surveys in the literature is presented in Shull, Danforth & Tilton (2014).

#### 4.2.1. O VI

The O VI  $1031.93, 1037.62 \text{ \AA}$  doublet is a strong ( $f = 0.1325, 0.0658$ ), resonance ( $2s - 2p$ ) transition of lithium-like oxygen. O VI receives a great deal of attention not only because it is the most commonly seen metal ion in the low-redshift IGM and CGM, but because it is thought to be a tracer of the warm-hot intergalactic medium (WHIM) at  $T > 10^5 \text{ K}$  (Tripp et al. 2001; Danforth & Shull 2005, 2008; Thom & Chen 2008; Danforth 2009). High-quality COS observations of O VI and H I absorbers have been used to constrain the physical properties in a number of IGM systems already (Savage et al. 2010, 2014; Stocke et al. 2014; Muzahid et al. 2015). Galaxy redshift surveys around IGM sight lines (Stocke et al. 2006; Chen & Mulchaey 2009; Prochaska et al. 2011; Johnson, Chen, & Mulchaey 2015) have shown that O VI systems are found  $\lesssim 1 \text{ Mpc}$  from the nearest  $L^*$  galaxies and thus closer to galaxies than typical Ly $\alpha$  forest lines. Studies of strong O VI systems ( $\log N_{\text{OVI}} \gtrsim 14.3$ ) in low-S/N COS data (e.g. the COS-Halos project Tumlinson et al. 2011, 2013) have shown a strong correlation between the specific star formation rate and the presence of O VI.

O VI absorption is detected in COS/FUV data at  $0.1 \lesssim z \lesssim 0.74$  because the G130M grating is only sensitive at  $\lambda \gtrsim 1135 \text{ \AA}$  and G160M ends at  $1796 \text{ \AA}$ . We find 280 O VI systems out of a total of 1658 IGM systems in this redshift range ( $\sim 17\%$ ). This is a factor of two more O VI systems than the Tilton et al. (2012) synthesis of STIS and *FUSE* surveys, enabling us to address the low- $z$  O VI properties with more statistical rigor. Observational O VI results are shown in Figure 9. For comparison, we include equivalent values derived from the Tilton et al. (2012) absorber list. In this and all subsequent plots that show absorbers from that study, we have combined all components within  $30 \text{ km s}^{-1}$  of each other to create absorption systems analogous to those we use in the COS survey.

The left panel of Figure 10 shows that O VI and H I column densities are essentially uncorrelated. What’s more, we see O VI systems ranging over a factor of

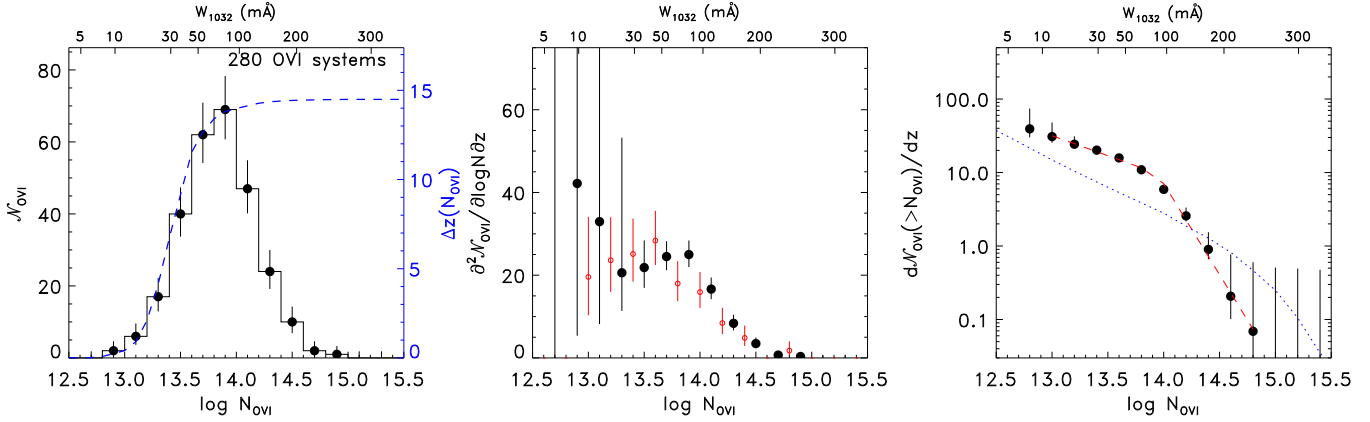


FIG. 9.— Statistics of 280 O VI systems in the COS IGM survey. The left panel shows the number  $N_{\text{OVI}}$  of absorbers per 0.2 dex column density bin. Error bars are one-sided Poisson uncertainties corresponding to  $\pm 1\sigma$ . Completeness is shown in the form of total pathlength  $\Delta z(N_{\text{OVI}})$  (dashed blue line, right axis). Approximate equivalent width in the stronger line of the doublet is given on the top axis. The middle panel shows the differential frequency of absorbing systems  $\partial^2 \mathcal{N} / \partial \log N \partial z$ . Open, red points show the corresponding distribution in the FUSE+STIS sample presented in Tilton et al. (2012) but post-processed to use the same convention of systems we use here. Right panel shows the cumulative frequency  $dN(>N)/dz$ . A single power law clearly does not represent the data, but a broken power law (red dashed line) with parameters  $\beta_{\text{strong}} = 2.5 \pm 0.2$ ,  $\beta_{\text{weak}} = 0.56 \pm 0.16$ ,  $\log N_{\text{break}} = 14.0 \pm 0.1$ ,  $C_{\text{break}} = 9.9 \pm 1.4$  provides a statistically better fit. A distribution from a cosmological simulation Smith et al. (2011) is shown as a blue dotted line in the right panel.

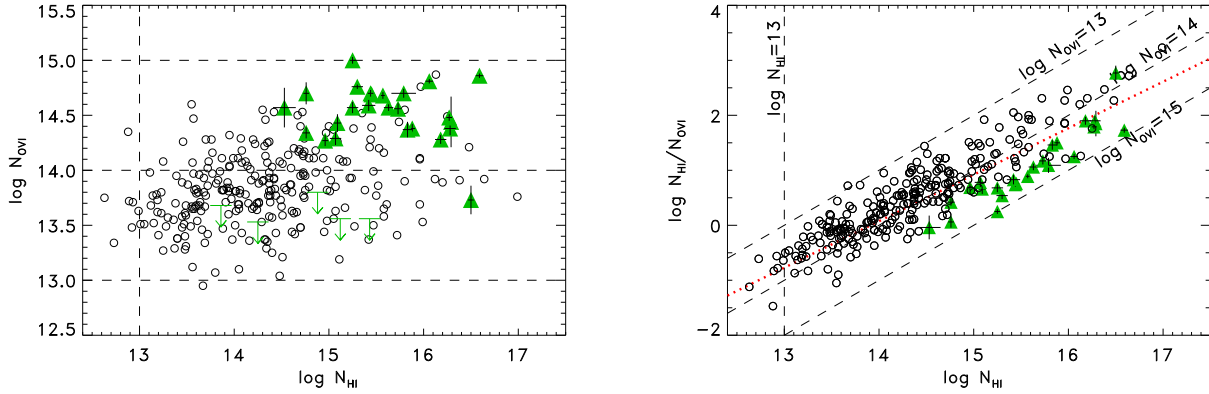


FIG. 10.— Column densities of HI and O VI are poorly correlated (left panel). Green triangles show the absorbers from the COS-Halos survey (Tumlinson et al. 2011). The fact that COS-Halos points occupy only one region of the larger parameter space suggests that not all O VI absorption is associated with the halos of  $L^*$  galaxies. The multiphase ratio  $N_{\text{HI}}/N_{\text{OVI}}$  in the right panel as a function of  $N_{\text{HI}}$  shows the poor column density correlation between neutral and highly-ionized systems which are kinematically related. Dashed lines show values of constant  $N_{\text{OVI}}$  and  $N_{\text{HI}}$ . A power-law fit to the data (red dotted line) has index  $0.86 \pm 0.01$  showing that the two column densities are poorly correlated. Components with  $N_{\text{OVI}} \lesssim 10^{13} \text{ cm}^{-2}$  are not typically detectable at our survey S/N.

$\sim 100$  in column density ( $13 \lesssim \log N_{\text{OVI}} < 15$ ) while the H I column density varies by a factor of  $10^6$  in this survey ( $12 < \log N_{\text{HI}} < 18$ ) but has been observed at much higher column densities in other extragalactic contexts. This lack of correlation has been noted before (Danforth & Shull 2005) where we defined a multiphase ratio,  $N_{\text{HI}}/N_{\text{OVI}}$ , to track the relative amounts of warm, photoionized and highly-ionized gas which often are kinematically associated. The right panel of Figure 10 shows the multiphase ratio as a function of H I column density. Because of S/N limitations, we are not sensitive to the weakest systems, which imposes approximate sensitivity limits  $N \gtrsim 10^{13} \text{ cm}^{-2}$  for both O VI and H I (upper dashed line in Figure 10). However, we see a sharp lower bound to the multiphase ratio, implying a maximum O VI column density of a few times  $10^{14} \text{ cm}^{-2}$  which is only weakly correlated with  $N_{\text{HI}}$ . A

fit to the multiphase ratio (dotted line) shows the relationship  $N_{\text{HI}}/N_{\text{OVI}} \propto (N_{\text{HI}}/10^{14} \text{ cm}^{-2})^{0.86 \pm 0.01}$ . This slope is consistent with that of Danforth & Shull (2005) who found  $N_{\text{HI}}/N_{\text{OVI}} \propto N_{\text{HI}}^{0.9 \pm 0.1}$ .

Green triangles in Figure 10 show the equivalent measurements drawn from the COS-Halos survey (Tumlinson et al. 2011). These are absorbing systems associated with the halos of large ( $> L^*$ ) star-forming galaxies. The COS-Halos surveys were not as sensitive to column densities of H I or O VI as is the current survey, but it is apparent that most star-forming galaxies can be associated with O VI absorption. However Stocke et al. (2006) find strong O VI absorbers at impact parameters out to  $\sim 0.8 \text{ Mpc}$  which is  $2-3 R_{\text{vir}}$  for  $L > L^*$  galaxies. So, while  $L^*$  galaxies have strong O VI absorption, the converse is not necessarily true.

Calculating  $dN/dz$  for O VI in the same manner as we

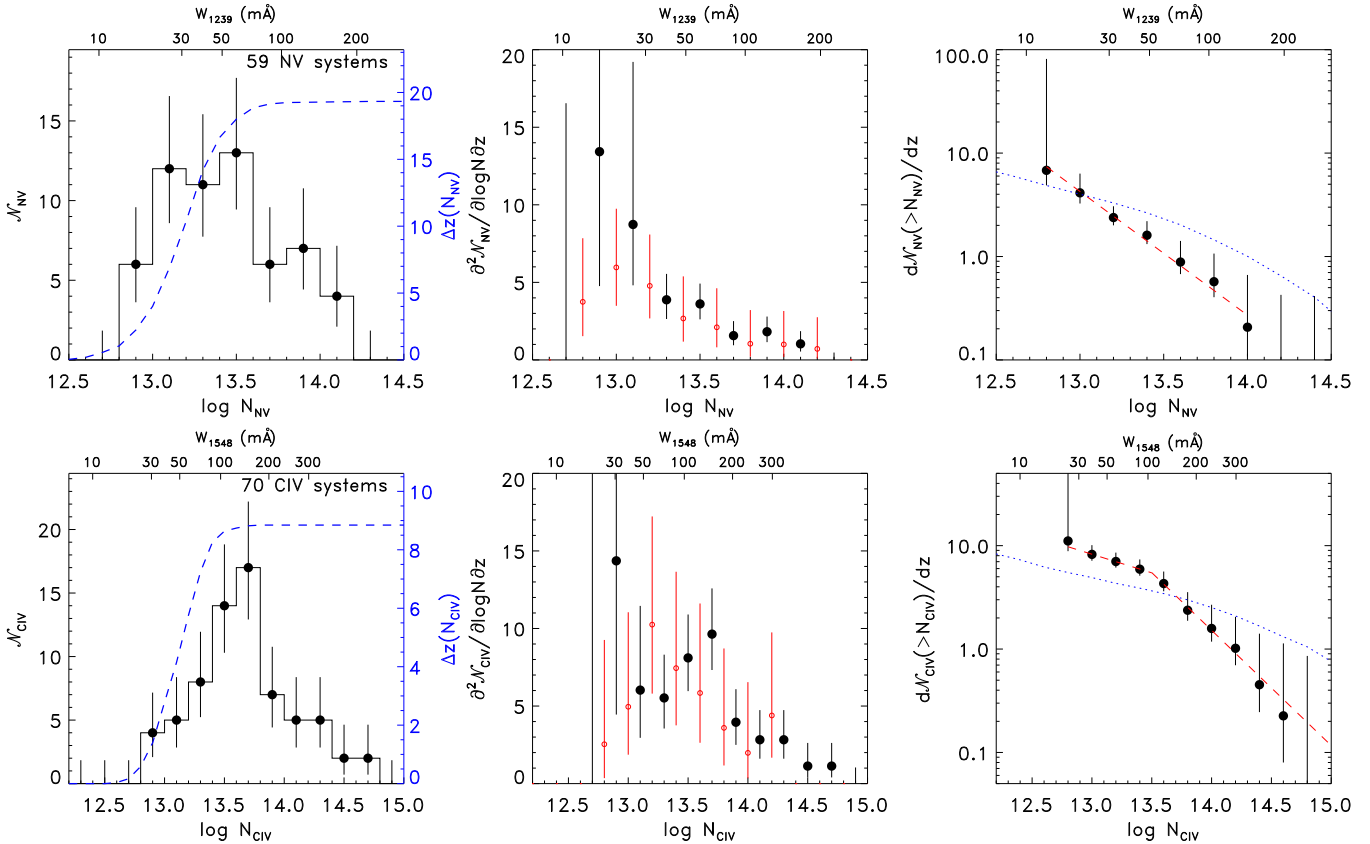


FIG. 11.— Same as Figure 9 but for 59 N V systems (top panels) and 70 C IV systems (bottom panels).

used in Section 4.1 for H I, we see a distinct “knee” in the distribution at  $\log N \approx 14$  (Figure 9, right panel). A broken power-law fit to the cumulative distribution of O VI absorbers (dashed curve) shows a break at  $\log N = 13.9 \pm 0.1$  with indices  $\beta_{\text{weak}} = 0.55 \pm 0.16$  and  $\beta_{\text{strong}} = 2.5 \pm 0.2$  and a normalization at the break of  $C_{\text{break}} = 9.7 \pm 1.3$ . There is curvature in the distribution not accounted for in the fit. A power-law fit is probably not the most appropriate in this context, but we present it here for comparison with theory and previous observational work. This two-slope distribution is in marked contrast with the results of DS08 who fitted the entire distribution (comprised of only 83 O VI absorbers) with a single power-law with  $\beta \sim 2.0$  over the range  $13.2 < \log N_{\text{OVI}} < 14.8$ .

We note that the slope break at  $\log N \approx 14$  is the dividing line of the population of circumgalactic O VI absorbers seen in the large COS-HALOS project. Tumlinson et al. (2011) find a strong correlation between star-forming galaxy halos and O VI absorption at  $\log N_{\text{OVI}} \gtrsim 14.2$ , while passive red galaxies tend to have O VI upper limits at this level or below. The weaker systems seen in this and previous surveys may correspond to more diffuse gas, possibly intra-group (Stocke et al. 2014) or a true intergalactic medium. “Circumgalactic” O VI gas may lie outside the virial radius of galaxies and still be flowing out to enrich the IGM (Stocke et al. 2006, 2013; Shull 2014).

#### 4.2.2. C IV and N V

O VI, N V and C IV are all lithium-like tracers of highly-ionized gas, which is either collisionally ionized to  $T \gtrsim 10^5$  K or photoionized by photons with  $\sim 50 - 100$  eV. Due to the lower cosmic abundances of carbon and nitrogen, as well as the limited redshift range over which C IV can be observed in COS/FUV spectra ( $z_{\text{abs}} \lesssim 0.16$ ), the number of IGM systems in which these ions are observed (N V: 59 systems, C IV: 70 systems) is considerably smaller than the 280 detected in O VI. Nevertheless, this is larger than previous surveys of these two ions in the low-redshift IGM. Both species appear to follow similar distributions to O VI, though without as much sensitivity to the weaker absorbers (Figure 11). The N V distribution is consistent with a single power law with index  $\beta = 2.2 \pm 0.1$  and normalization  $C_{14} = 0.3$ . The cumulative distribution of C IV shows a clear turnover and is fitted with a broken power law ( $\beta_{\text{weak}} = 1.4 \pm 0.3$  and  $\beta_{\text{strong}} = 2.1 \pm 0.3$ ) with a break at  $\log N_{\text{CIV}} = 13.5 \pm 0.2$  and normalization  $C_{\text{break}} = 5.5 \pm 1.5$ .

#### 4.2.3. Si III, C III, and Si IV

Si III and C III absorbers are relatively common in the IGM owing to the very high oscillator strengths of the 1206.5 Å ( $f = 1.63$ ) and 977.0 Å ( $f = 0.757$ ) transitions, respectively. These systems in previous studies trace H I systems to a much better extent than more highly-ionized species, probably because C III and Si III trace photoionized gas. We detect Si III and/or C III absorption in 200 systems. The Si IV doublet ( $\lambda 1393.76, 1402.70$ ) is also relatively strong, though the decreased abundance of Si compared with cosmic C/N/O means

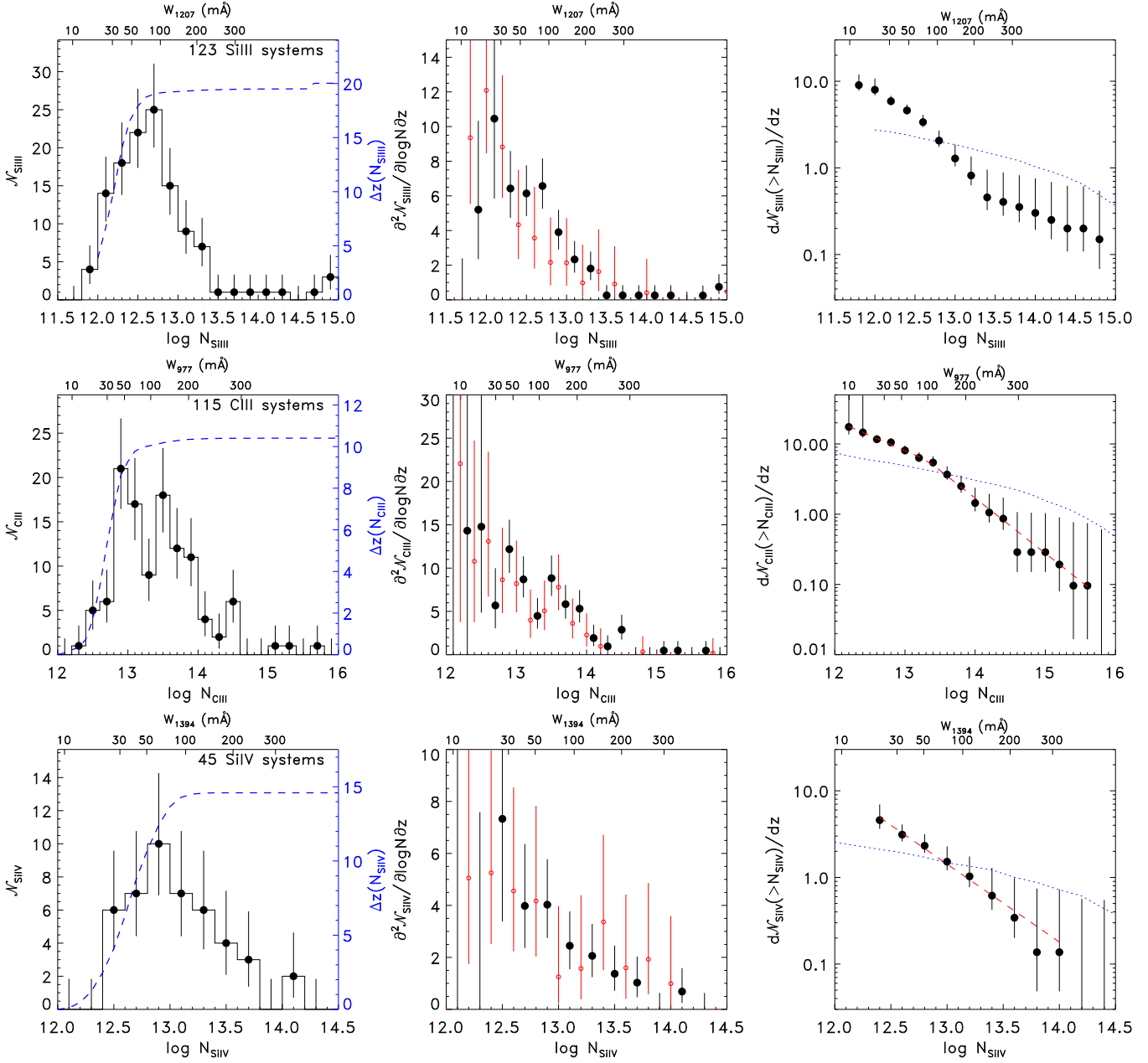


FIG. 12.— Same as Figure 9 for 123 Si III systems (top panels), 115 C III systems (middle panels), and 45 Si IV systems (bottom panels).

that these absorbers are somewhat less common; only 45 Si IV systems are seen in this survey for a line frequency  $dN/dz \sim 3$  for components with  $W_\lambda \gtrsim 30$  mÅ.

Si III, with an ionization range of 16.3–30.7 eV, traces low-ionization, metal-enriched gas, while C III (24.4–47.9 eV) and Si IV (33.5–45.1 eV) trace an ionization middle-ground between Si III and the high-ionization species such as C IV, N V, and O VI (50–150 eV). The  $dN/dz$  distribution of all three lower-ionization species is consistent with that seen in previous surveys (Figure 12). The Si IV distribution is fitted with  $\beta = 1.9 \pm 0.2$ ,  $C_{14} = 0.2$  for  $\log N_{\text{SiIV}} \leq 14.1$ . C III is reasonably fit with a two-slope power law ( $\beta_{\text{weak}} = 1.4 \pm 0.1$  and  $\beta_{\text{strong}} = 1.81 \pm 0.1$ ) with a break at  $\log N_{\text{break}} = 13.3 \pm 0.3$  and normalization at the break of  $C_{\text{break}} = 5.9 \pm 1.6$ . Si III does not follow an obvious power-law distribution.

#### 4.2.4. Are the $dN/dz$ turnovers real?

The distributions of many of the metal ions shown in Figures 9–12, particularly O VI, C IV, and C III, show a clear flattening in their numbers at lower column densities. Because weaker systems are observed over smaller effective pathlengths, we investigated whether this apparent flattening in the  $dN/dz$  values at lower column densities could be an effect of completeness. The nominal  $\Delta z(N)$  function (e.g., blue curve in Fig. 9) is calculated for  $3\sigma$  detections. If this threshold is raised to  $4\sigma$  or even  $5\sigma$ , there is relatively less effective pathlength at lower column densities. The blue curve in the left-hand panels of Figures 9, 11, 12 representing  $\Delta z(N)$  moves to the right by  $\sim 0.1$  dex for each  $1\sigma$  increase in significance level and the frequency of weak absorbers rises. This results in a steepening of the weak-end slope of the

cumulative distribution function (less pathlength for the same number of detections), but it does not eliminate the non-power-law nature of the distributions in any case. Therefore, we believe that the turnovers seen in many of the metal absorber distributions are real, but the weak-end slopes should be treated with caution.

#### 4.2.5. *Ne VIII*

The extreme-UV (2s-2p) doublet transition of Ne VIII ( $\lambda = 770.41, 780.32 \text{ \AA}$ ,  $f = 0.1030, 0.0505$ ) is often presented as a less-ambiguous tracer of collisionally-ionized gas than O VI or other highly-ionized, FUV metal transitions (Savage et al. 2005). Several compelling studies of warm-hot or multi-phase gas have been made using Ne VIII in conjunction with H I, O VI, and other ions to constrain gas temperature and density (Savage et al. 2005, 2011; Narayanan et al. 2009, 2011; Tripp et al. 2011; Meiring et al. 2013; Hussain et al. 2015). Unfortunately, the Ne VIII doublet only redshifts into the COS/G130M band at  $z \gtrsim 0.47$ , which limits us to the 13 highest-redshift AGN sight lines in this survey, usually without observations of the strong H I counterparts. We measure several dozen Ne VIII systems, but all are at redshifts similar to the background AGN and show the hallmarks of intrinsic, rather than intervening, absorption. They are primarily strong, blended, multi-component absorption profiles in high ions, often lacking H I absorption.

There are three Ne VIII detections at  $> 3\sigma$  in our survey which can be reasonably identified as intergalactic rather than intrinsic systems. The system detected toward PKS 0405–123 at  $z = 0.49494$  in Ne VIII and O VI by Narayanan et al. (2011) shows  $\log N_{\text{NeVIII}} = 13.5 \pm 0.2$  and  $\log N_{\text{OVI}} = 14.32 \pm 0.05$ . In an earlier reduction of the data allowing for the contaminating effects of fixed pattern noise, Narayanan et al. (2011) measured column densities of  $\log N_{\text{NeVIII}} = 13.96 \pm 0.06$  and  $\log N_{\text{OVI}} = 14.39 \pm 0.01$ . The origin of the Ne VIII and O VI is consistent with collisionally ionized gas with  $T \approx 5 \times 10^5 \text{ K}$  and a baryonic column density of  $N_H \sim 10^{19} - 10^{20} \text{ cm}^{-2}$ .

Two other Ne VIII detections have no corresponding absorption in any other metal or H I transition. The first is a pair of broad absorption features toward PKS 0637–752 consistent with Ne VIII doublet absorption at  $z = 0.60552$  with  $\log N_{\text{NeVIII}} = 14.0$ . Ly $\beta$  and O VI  $\lambda 1032$  non-detections place  $3\sigma$  column density upper limits of  $\log N_{\text{HI}} \leq 13.6$  and  $\log N_{\text{OVI}} \leq 13.4$ , respectively. A similar pair of weak absorption features in the HE 0238–1904 sight line is consistent with a  $z = 0.50511$  Ne VIII doublet:  $\log N_{\text{NeVIII}} = 14.1$ ,  $\log N_{\text{HI}} \leq 13.4$ , and  $\log N_{\text{OVI}} \leq 13.2$ . These two Ne VIII-only systems provide interesting limits on the temperature of the absorbing gas. If in collisional ionization equilibrium (CIE) and with the solar Ne/O abundance, the O VI non-detections imply a gas temperature of  $T \gtrsim 3 \times 10^6 \text{ K}$ . This is consistent with the broad line profiles observed in the Ne VIII lines ( $b_{\text{thermal}} \sim 50 \text{ km s}^{-1}$ ) and the H I non-detection.

The effective pathlength for Ne VIII systems with  $N_{\text{NeVIII}} \approx 10^{14} \text{ cm}^{-2}$  in our survey is only  $\Delta z \sim 2$ , quite small compared with the other species presented here. With only three significant detections over this pathlength, only one of which is confirmed with absorp-

tion in other species, it is clear that Ne VIII absorbers detectable in data of modest S/N are rare. Based on the detection of three Ne VIII/O VI systems in the high-S/N spectrum of PG 1148+549 ( $z_{\text{em}} = 0.9754$ ), Meiring et al. (2013) estimate  $dN/dz = 7_{-3}^{+7}$  for Ne VIII systems with  $W_r > 30 \text{ m\AA}$ . Our modest-S/N finds  $dN/dz \sim 3$  with large uncertainties for Ne VIII systems with  $W_r > 30 \text{ m\AA}$ . Effective surveys for a statistical sample of Ne VIII systems will require high-S/N observations of AGN at redshifts of  $z \sim 1$  or a deeper survey at slightly lower redshifts ( $z_{\text{NeVIII}} \gtrsim 0.41$ ) with the COS G130M/1222 setting.

#### 4.3. *Baryon Census*

The majority of baryons at *all* epochs are not in the form of virialized, luminous matter (Shull, Smith, & Danforth 2012). Thus observations of the diffuse IGM are the most effective way of tracking the majority of normal matter across the history of the universe. As in previous papers (Danforth & Shull 2005, 2008; Tilton et al. 2012), we calculate the baryon content of the IGM systems, here observed with COS. We compute two quantities:  $\Omega_{\text{ion}}$ , the contribution to closure density by a particular element and ionization stage; and  $\Omega_{\text{IGM}}^{(\text{ion})}$  which estimates the fraction of closure density represented by all the gas traced by absorption in a particular species.  $\Omega_{\text{ion}}$  is a purely-observational quantity with no corrections, while  $\Omega_{\text{IGM}}^{(\text{ion})}$  must include assumptions about metallicity ( $Z/Z_{\odot}$ ), solar elemental abundance  $(M/H)_{\odot}$ , and ion fraction ( $f_{\text{ion}}$ ).

A full discussion of our methodology is presented in Section 2.4.1 of Tilton et al. (2012) from which we use Eq. (5) to calculate  $\Omega_{\text{ion}}$

$$\Omega_{\text{ion}} = (1.365 \times 10^{-23} \text{ cm}^2 h_{70}^{-1} (m_{\text{ion}}/\text{amu}) \times \sum_{i=\log N_{\text{min}}}^{\log N_{\text{max}}} \left[ \frac{\partial^2 \mathcal{N}(\log N)}{\partial \log N \partial z} \right]_i \langle N_i \rangle \Delta \log N_i. \quad (4)$$

For metal ions, we calculate  $\Omega_{\text{IGM}}^{(\text{ion})}$  via Eq. (6) of Tilton et al. (2012)

$$\Omega_{\text{IGM}}^{(\text{ion})} = \frac{1.83 \times 10^{-23} h_{70}^{-1} \text{ cm}^2}{f_{\text{ion}}(Z/Z_{\odot}) (M/H)_{\odot}} \times \sum_{i=N_{\text{min}}}^{N_{\text{max}}} \left[ \frac{\partial^2 \mathcal{N}(\log N)}{\partial \log N \partial z} \right]_i \langle N_i \rangle \Delta \log N_i. \quad (5)$$

Instead of assuming a constant metallicity  $Z$  and ion fraction  $f_{\text{ion}}$  as we have done in previous calculations (Penton, Stocke, & Shull 2004; Danforth & Shull 2005, 2008), we take advantage of the covariance of the product  $f_{\text{ion}}(Z/Z_{\odot})$  seen in cosmological simulations. We used parameterized fits of the form  $f_{\text{ion}}(Z/Z_{\odot}) = A(N_{\text{ion}}/10^{14} \text{ cm}^{-2})^B$ . Parametric coefficients for the species are as follows: O VI: A=0.015, B=0.700 (Shull, Smith, & Danforth 2012); N V: A=0.036, B=0.617; C IV: A=0.009, B=0.690 (B. Smith, 2013, priv. comm.).

The baryon fraction traced by photoionized H I absorbers in the Ly $\alpha$  forest  $\Omega_{\text{IGM}}^{(\text{HI})}$  is calculated via Eq. (10)

of Tilton et al. (2012)

$$\Omega_{\text{IGM}}^{(\text{HI})}(z) = (9.0 \times 10^{-5}) h_{70}^{-1} p_{100}^{1/2} T_{4.3}^{0.363} \times \frac{(1+z)^{0.2}}{[\Omega_m(1+z)^3 + \Omega_\Lambda]^{1/2}} \times \sum_{i=N_{\text{min}}}^{N_{\text{max}}} \left[ \frac{\partial^2 \mathcal{N}(\log N)}{\partial \log N \partial z} \right]_i \Delta \log N_i \left( \frac{\langle N_i \rangle}{10^{14} \text{ cm}^{-2}} \right)^{1/2} \quad (6)$$

where the temperature  $T$  is normalized at 20,000 K, column density is in units of  $10^{14} \text{ cm}^{-2}$ , and the AGN sight line impact parameter  $p_{100}$  is normalized to 100 kpc. See full discussion in Tilton et al. (2012) and Shull, Smith, & Danforth (2012).

We calculate  $\Omega_{\text{ion}}$  and  $\Omega_{\text{IGM}}^{(\text{ion})}$  values for H I, O VI, N V and C IV (Table 6). Uncertainties are the per-bin errors added in quadrature. The dominant source of random error for all  $\Omega$  calculations is small number statistics. For this reason we sum over the column density range of typical, weak and moderate lines ( $N_{\text{HI}} < 10^{16} \text{ cm}^{-2}$ ,  $N_{\text{metal}} < 10^{15} \text{ cm}^{-2}$ ) and do not include the rare, high-column density absorbers. These may add an additional 6 – 8% to  $\Omega_b^{(\text{HI})}$ . The lower limit to the column density range is observationally motivated and corresponds to  $W_r = 30 \text{ m}\text{\AA}$ . The sample of H I absorbers is large enough to divide the sample into redshift bins of  $\Delta z \approx 0.1$  and maintain reasonable statistics. Metal ions lack sufficient detections to subdivide the same way, and thus  $\Omega_{\text{ion}}$  and  $\Omega_{\text{IGM}}^{(\text{ion})}$  for each metal ion are calculated over a single redshift range.

The  $\Omega_b$  analysis finds that the photoionized Ly $\alpha$  forest at  $z \lesssim 0.5$  can account for  $\sim 20 - 25\%$  of the baryons while WHIM gas as traced by O VI can account for  $\sim 11\%$ . These fractions are smaller than those found in our previous surveys (Penton, Stocke, & Shull 2004; Danforth & Shull 2005, 2008) since we use the more realistic ionization corrections and  $f_{\text{ion}}(Z/Z_\odot)$  method described above while previous surveys used a

constant metallicity  $Z/Z_\odot = 10\%$  and an ionization fraction near the peak of the CIE abundance for that ion. However, these results are consistent with those of Tilton et al. (2012) and Shull, Danforth & Tilton (2014) both of which apply the same covariance technique applied here to the STIS and FUSE data of Tilton et al. (2012). For a more detailed comparison of the evolution of  $\Omega_{\text{metal}}$  in the IGM with previous work including higher-redshift studies (see Shull, Danforth & Tilton 2014).

#### 4.4. Metal-ion Abundances

Over the past two decades, there have been numerous studies of the metallicity evolution of the IGM, probed by the strong metal-ion absorbers in the rest-frame ultraviolet (C IV, Si IV, O VI, and a few others). These metal abundances are parameterized by their densities relative to the cosmological closure density, for example  $\Omega_{\text{CIV}}$ . Shull, Danforth & Tilton (2014) discussed the metal-line measurements from 49 low-redshift ( $z < 0.4$ ) HST/COS absorbers to find  $\Omega_{\text{CIV}} = 10.1_{-2.4}^{+5.6} \times 10^{-8} (h_{70}^{-1})$ . In their Table 2, they compare this value to updated measurements from HST/STIS (Tilton et al. 2012). The Tilton et al. (2012) number was revised by Shull, Danforth & Tilton (2014) to  $\Omega_{\text{CIV}} = 8.1_{-1.7}^{+4.6} \times 10^{-8} h_{70}^{-1}$  which is not statistically different from the COS measurement. The adjustments were based on three corrections to the method: (1) computation of absorbers over a consistent range of column density ( $12.87 < \log N_{\text{CIV}} < 14.87$ ); (2) re-evaluation of the absorber sensitivity and effective redshift pathlength; (3) fitting the distribution  $f(N, z)$  to an analytic form and integrating over the assumed column-density range. The first restriction eliminated a few strong, uncertain absorbers that biased the computation. The second and third adjustments resulted in a more robust computation, as discussed extensively in Section 2.2 and Table 2 of Shull, Danforth & Tilton (2014). There is now general agreement on the low-redshift value for the C IV metal abundance,  $\Omega_{\text{CIV}} \sim 10^{-7} (H_{70})^{-1}$ .

TABLE 6  
 $\Omega$  VALUES

Species	$\log N^a$	$z_{\text{abs}}$	$N_{\text{abs}}$	$\Omega_{\text{ion}}$ ( $\times 10^{-8}$ )	$\Omega_{\text{IGM}}^{(\text{ion})}$ ( $\times 10^{-3}$ )	$\Omega_{\text{IGM}}^{(\text{ion})}/\Omega_b^b$ (%)
HI	12.8 – 16	0 – 0.1	801	$18.01_{-2.06}^{+2.49}$	$7.70_{-0.38}^{+0.43}$	$16.9_{-0.8}^{+0.9}$
HI	12.8 – 16	0.1 – 0.2	660	$24.14_{-3.36}^{+4.21}$	$8.82_{-0.51}^{+0.60}$	$19.4_{-1.1}^{+1.3}$
HI	12.8 – 16	0.2 – 0.3	369	$20.89_{-3.49}^{+4.69}$	$8.14_{-0.58}^{+0.71}$	$17.9_{-1.3}^{+1.6}$
HI	12.8 – 16	0.3 – 0.4	262	$32.95_{-5.59}^{+7.34}$	$11.66_{-0.95}^{+1.18}$	$25.6_{-2.1}^{+2.6}$
HI	12.8 – 16	0.4 – 0.47	140	$40.47_{-9.80}^{+14.66}$	$14.19_{-1.66}^{+2.32}$	$31.2_{-3.7}^{+5.1}$
HI	12.8 – 16	0 – 0.4	2092	$24.00_{-3.84}^{+4.99}$	$9.08_{-0.64}^{+0.78}$	$20.0_{-1.4}^{+1.7}$
O VI	13.4 – 15	0.1 – 0.75	255	$40.37_{-3.07}^{+4.54}$	$4.96_{-0.31}^{+0.37}$	$10.9_{-0.7}^{+0.8}$
N V	13.2 – 15	0 – 0.45	46	$2.10_{-0.35}^{+0.53}$	$1.57_{-0.23}^{+0.32}$	$3.4_{-0.5}^{+0.7}$
C IV	12.9 – 15	0 – 0.16	68	$9.89_{-1.73}^{+3.24}$	$3.63_{-0.45}^{+0.71}$	$8.0_{-1.0}^{+1.6}$

<sup>a</sup> Additional baryons may be present outside the range ( $12.8 \leq \log N_{\text{HI}} \leq 16.0$ ) listed here.

<sup>b</sup>  $\Omega_b = 0.0455 \pm 0.0028$  (Larson et al. 2011).

## 5. DISCUSSION

5.1. Evolution of the Low- $z$  IGM

The COS IGM survey samples a large fraction of the history of the universe with a statistically-significant number of absorbers seen along many sight lines. Our Ly $\alpha$  forest sensitivity with the COS G130M/G160M gratings ends at  $z \approx 0.47$ , equivalent to a lookback time of 4.9 Gyr or 35% of the age of the universe, so it is logical to look for changes in the overall sample properties (such as  $dN/dz$ ) over that time. The sight lines are biased toward low-redshift AGN targets (median  $z_{\text{AGN}} = 0.19$ ) and the absorbers are similarly biased toward lower redshifts (the median and  $\pm 1\sigma$  redshift sensitivity of our survey is  $z_{\text{abs}} = 0.14_{-0.10}^{+0.19}$ ). We calculate effective pathlength as a function of column density as above, but use only the portion of each sight line which probes a particular redshift range. A limit and final point are included in Figure 13 the bin at  $0.47 < z < 0.75$  in which systems are found via Ly $\beta$  and Ly $\gamma$  absorption. However, the uncertainties in pathlength for this range, as well as the small sample size in this redshift bin, make any firm conclusions beyond  $z \approx 0.47$  difficult.

The left panel of Figure 13 shows how the observed  $dN/dz$  changes as a function of redshift in our sample. We fit the cumulative frequency of lines above a certain column density as  $dN(> N, z)/dz = C_0 (1+z)^\gamma$ . The strong sample ( $N_{\text{HI}} > 10^{14} \text{ cm}^{-2}$ ) shows clear evolution with  $\gamma = 2.3 \pm 0.1$ ,  $C_0 = 16 \pm 1$ . Evolution in the weaker sample ( $10^{13} \text{ cm}^{-2} < N_{\text{HI}} < 10^{14} \text{ cm}^{-2}$ ) can be fitted with  $\gamma = 1.15 \pm 0.05$ ,  $C_0 = 74 \pm 1$ , but there is an increase in weak systems at  $z \gtrsim 0.3$ , which suggests that a simple power law may not be appropriate for weak system evolution. The observed  $\gamma > 0$  means that the frequency of IGM absorbers is lower at  $z = 0$  than at higher redshift, while the difference  $\Delta\gamma \approx 1$  between strong and weak systems means that weaker systems become relatively more dominant at lower redshifts. A fit to the  $N_{\text{HI}} \geq 10^{13} \text{ cm}^{-2}$  sample gives  $\gamma = 1.24 \pm 0.06$  and  $C_0 = 91 \pm 1$ .

The difference in evolution indices  $\gamma$  for strong and weak H I systems implies that the slope  $\beta$  of the  $dN/dz$  distribution should become steeper with decreasing  $z$ . This is observed in the data as well (right panel of Figure 13). The evolution at  $z \leq 0.47$  of systems in the range  $13 \leq \log N_{\text{HI}} < 17$  is fitted by  $\beta(z) = (1.70 \pm 0.01) - (0.15 \pm 0.06)z$ . However, given the heterogenous method of H I column density determination between the  $z < 0.1$  and  $z > 0.1$  systems, we prefer the steeper fit  $\beta(z) = (1.75 \pm 0.03) - (0.31 \pm 0.10)z$  (dashed red line).

In a comparable set of IGM observations at with HST/STIS in the near-UV, Janknecht et al. (2006) measured  $\beta = 1.60 \pm 0.03$  for IGM absorbers at  $0.5 < z < 1.9$ . Rudie et al. (2013) find  $\beta = 1.65 \pm 0.02$  for  $\log N > 13.5$  H I absorbers at  $z \sim 2 - 3$ . However, they note that the slope is shallower ( $\beta = 1.447 \pm 0.033$ ) for absorbers within  $700 \text{ km s}^{-1}$  of a galaxy, which they interpret as circumgalactic gas rather than IGM. Extrapolating the low- $z$  fit to the redshifts of the comparable near-UV and optical studies produces slopes much shallower than are observed;  $\beta(z = 1) \approx 1.4$ ,  $\beta(z = 2.5) \approx 1.0$ . Thus, our linear relationship should not be extrapolated to redshifts beyond  $z \approx 0.5$ .

We can now modify Eq. (3) to

$$\frac{dN(> N, z)}{dz} = C_0 (1+z)^\gamma \left( \frac{N}{10^{14} \text{ cm}^{-2}} \right)^{-[\beta(z)-1]} \quad (7)$$

Here we adopt  $C_{14,0} = 16$  and  $\gamma = 2.3$ , and the second fit,  $\beta(z) = 1.75 - 0.31z$ , which predicts stronger evolution. Theoretically, we would expect the Ly $\alpha$  forest to evolve with redshift due to the rapid drop in photoionizing background at  $z < 2$  and the evolution of density and mass in the large-scale structure of the gaseous filaments. Because the H I neutral fraction depends on the ratio of ionizing flux to density (the photoionization parameter  $U$ ), the H I fraction will evolve in redshift, and the column-density distribution will shift (Davé et al. 2010; Smith et al. 2011; Penton, Stocke, & Shull 2004).

5.1.1. The Ly $\alpha$  Decrement

Another way of assessing the evolution of the Ly $\alpha$  forest is to measure the Ly $\alpha$  decrement  $D_A(z)$ ,

$$D_A(z) = \frac{\sum_i W_{r,i} (1+z_i)}{\lambda_0 \Delta z_i(z)}, \quad (8)$$

the fraction of light removed from the continuum by the Ly $\alpha$  forest at any given redshift. At high redshift, the decrement approaches 100%, but the modern universe is much more transparent to light at  $1215.67 \text{ \AA}$ . Measuring the Ly $\alpha$  decrement from the COS survey is a relatively simple matter. Each absorption component has a measured rest equivalent width  $W_{r,i}$ . Summing the observed equivalent widths  $W_{\text{obs}} = W_r (1+z)$ , of all the Ly $\alpha$  absorption components in a particular redshift range and then dividing by total clear path length  $\Delta z_i$  gives the decrement (Eq. 8).

The Ly $\alpha$  decrement is dominated by H I absorbers of column density  $13.5 < \log N_{\text{HI}} < 14.5$  which are both common and relatively strong. Figure 14 shows the decrement in  $\Delta z = 0.01$  bins (small open circles) and larger  $\Delta z = 0.05$  bins (filled circles). There is considerable variation from one redshift bin to the next, but the typical decrement is a few percent. The larger spread in data points at  $z \gtrsim 0.35$  is probably due to the increasing effects of cosmic variance as a result of the smaller number of sight lines probing this redshift range. A power law fit to the data gives  $D_A = (0.014 \pm 0.001) (1+z)^{2.2 \pm 0.2}$  and  $D_A = (0.013 \pm 0.001) (1+z)^{2.1 \pm 0.2}$  for the  $\Delta z = 0.05$  and  $\Delta z = 0.01$  binnings, respectively. This is significantly steeper than the fit of Kirkman et al. (2007) who used a pixel-optical-depth technique with data from HST/FOS to find  $D_A = 0.016 (1+z)^{1.01}$ .

The distribution of  $D_A(z)$  has been used as a constraint on the ionizing radiation field at redshifts  $z < 0.4$  (Shull et al. 2015). For absorbers that evolve in line frequency as  $(1+z)^\gamma$ , the flux decrement should increase with redshift as  $D_A \propto (1+z)^{\gamma+1}$ . The extra factor of  $(1+z)$  arises from the fact that the absorption-line equivalent width  $W_\lambda$  increases with  $(1+z)$ . We observe  $D_A \propto (1+z)^{2.1-2.2}$ , which is consistent with our index  $\gamma = 1.17 \pm 0.06$  for unsaturated lines ( $13 < \log N < 14$ ).

## 5.1.2. Metal Evolution

The sample of metal-line systems is much smaller than the IGM H I sample, but we can still use it to constrain

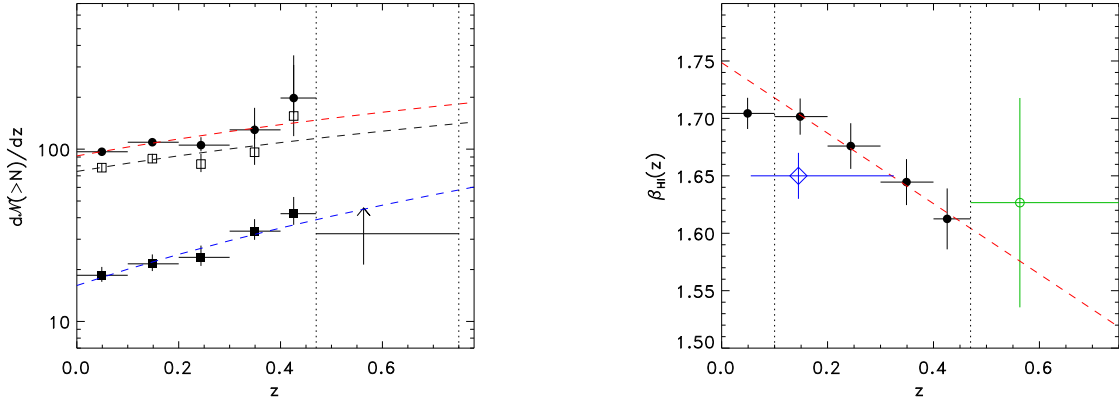


FIG. 13.— Evolution in the Ly $\alpha$  forest. Left panel: integrated  $dN/dz$  values for all ( $N_{\text{HI}} > 10^{13} \text{ cm}^{-2}$ , filled circles), strong ( $N_{\text{HI}} > 10^{14} \text{ cm}^{-2}$ , filled squares), and weak ( $10^{13} \text{ cm}^{-2} \leq N_{\text{HI}} < 10^{14} \text{ cm}^{-2}$ , open squares) HI systems as a function of redshift. The evolution of the stronger systems can be fitted by the relationship  $dN(>N, z)/dz = C_0(1+z)^\gamma$  with  $\gamma_{\text{strong}} = 2.3 \pm 0.1$ ,  $C_{0,\text{strong}} = 16 \pm 1$  (blue dashed line). The total and weaker distributions are fitted with  $\gamma_{\text{all}} = 1.24 \pm 0.04$ ,  $C_{0,\text{all}} = 91 \pm 1$  (red) and  $\gamma_{\text{weak}} = 1.15 \pm 0.06$ ,  $C_{0,\text{weak}} = 74 \pm 1$  (black). Vertical dotted lines show the redshift limits of the Ly $\alpha$  and Ly $\beta$  forests which can be observed in COS/FUV data. Right panel: power law index  $\beta(z)$  as a function of redshift. A linear fit to the  $0.1 < z_{\text{abs}} < 0.47$  bins (dashed red line) shows a steep evolution of  $\beta(z) = (1.75 \pm 0.03) - (0.31 \pm 0.10)z$ . A high-redshift ( $0.47 < z < 0.75$ , green circle) data point based on Ly $\beta$ +Ly $\gamma$  HI detections is included in the Figure, but not used in the fit. The full-sample value of  $\beta = 1.65 \pm 0.02$  is shown as a blue diamond at the median absorber redshift along with the  $\pm 1\sigma$  range.

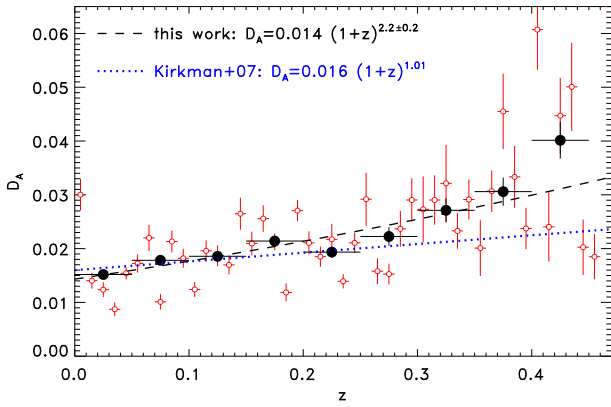


FIG. 14.— The observational Ly $\alpha$  decrement  $D_A$  as a function of redshift. The observed frame equivalent widths of all Ly $\alpha$  components within a particular redshift range are summed and divided by the clear pathlength in that range. Cosmic variance contributes significant scatter to  $D_A(z)$ , but the data, binned to  $\Delta z = 0.05$  (black data points), can be fitted with the form  $D_A = 0.014(1+z)^{2.2 \pm 0.2}$  (dashed line). The dotted line shows the HST/FOS fit of Kirkman et al. (2007);  $D_A = 0.016(1+z)^{1.01}$ .

the evolution of different metal-ion systems across a significant redshift range. We group metal systems into the same six redshift bins used for H I and measure the cumulative  $dN(>N)/dz$  at the observational threshold  $W \geq 30 \text{ m\AA}$  for metal species with both significant redshift coverage and detection statistics. The results are shown in Figure 15 for O VI, N V, C III, and Si III. C IV is sampled only over a small redshift range, and there are not enough Si IV detections to provide any reliable statistics when spread over multiple redshift bins. We follow the same procedure as used above for H I, calculating integrated  $dN/dz$  profiles in up to five redshift bins. O VI systems at  $z < 0.1$  and C III systems at  $z < 0.16$  are not observed in COS data, so comparable literature

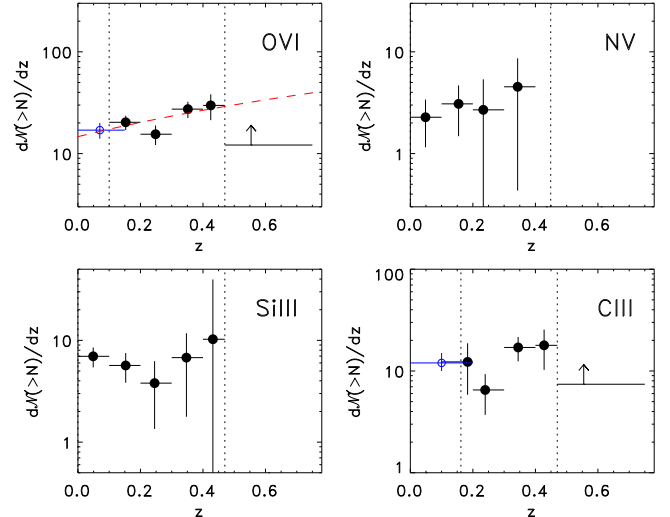


FIG. 15.— Evolution of metal systems in four species. Cumulative  $dN/dz$  as a function of redshift is shown for systems with rest-frame equivalent width  $W_\lambda > 30 \text{ m\AA}$ . Lower limits are shown with arrows. Vertical dotted lines indicate the redshift range over which the species appears in COS data. O VI (upper left) and C III (lower right) lack COS coverage at  $z_{\text{OVI}} < 0.10$  and  $z_{\text{CIII}} < 0.16$ , so literature values (blue, open symbols) from DS08 and references therein are plotted in place of the lowest-redshift bins. A dashed line shows the best fit to the O VI data; all other ions are consistent with no evolution.

values from Danforth & Shull (2005) and Danforth et al. (2006) are used for the lowest-redshift data point.

Statistics are poor even for O VI, the most numerous of the metal-ion detections. O VI appears to evolve with redshift in the same sense at H I. A fit of the form  $dN(>N)/dz \propto (1+z)^\gamma$  gives  $\gamma_{\text{OVI}} = 1.8 \pm 0.8$  at  $z < 0.47$  for  $W_\lambda > 30 \text{ m\AA}$  including the  $z < 0.16$  value from Danforth & Shull (2005) at the lowest redshift bin. Evolution in the other three ions is poorly constrained. N V is fitted with  $\gamma_{\text{NV}} = 2.4 \pm 2.9$ . Si III and C III,

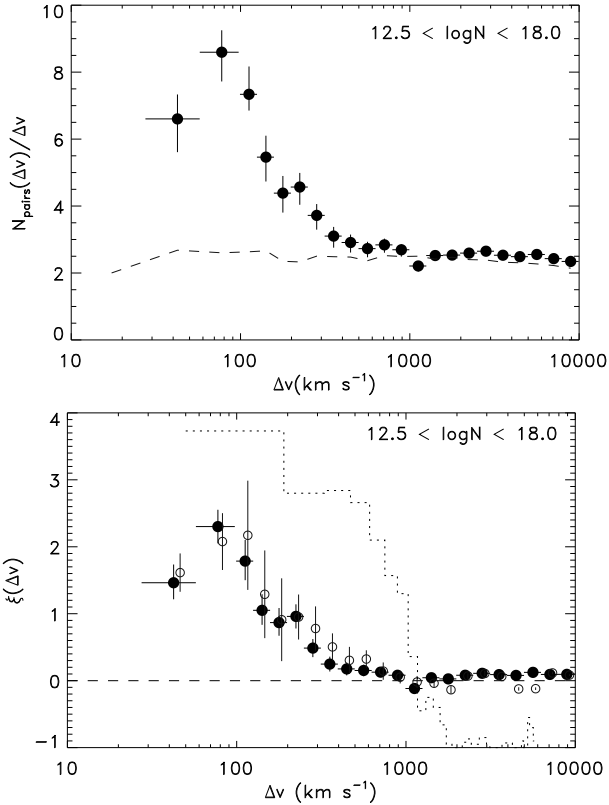


FIG. 16.— Two-point correlation function in the low- $z$  Ly $\alpha$  forest. Observed component pairs (top) show significant signal at  $\Delta v \sim 100 \text{ km s}^{-1}$  compared with a sample of randomly-placed components with the same overall  $dN/dz$  behavior (dashed line). The two-point correlation function,  $\xi(\Delta v)$  (bottom) shows the same clustering at  $\Delta v \sim 100 \text{ km s}^{-1}$ , and no clustering at higher velocity separations. This is in contrast to the TPCF of galaxies to galaxies (dotted line; Penton, Stocke, & Shull 2004) which showed significant correlation at  $\Delta v < 1000 \text{ km s}^{-1}$ . *HST*/STIS data from Tilton et al. (2012) show a similar behavior (open circles) including the smaller TPCF at low velocity separations.

which typically show properties correlated closely with H I (DS08), are also poorly constrained ( $\gamma_{\text{SIII}} = -1 \pm 2$ ,  $\gamma_{\text{CIII}} = 1.7 \pm 1.3$ ). Much larger samples of metal-ion absorbers are required before metal evolution can be measured with any precision.

### 5.2. Clustering of IGM Absorbers

The two-point correlation function (TPCF) and its amplitude  $\xi$  is often used as a measure of clustering in the universe (Peebles 1980). A value of  $\xi > 0$  means there is greater-than-random clustering, while  $\xi < 0$  may indicate anti-clustering (voids). Since our sight lines sample physically unrelated regions in almost all cases, we can use absorbers along them to measure the velocity-space clustering of absorbing materials in the IGM.

We calculate  $\xi(\Delta v)$  for Ly $\alpha$  components in each sight line as

$$\xi(\Delta v) = \frac{N_{\text{obs}}(\Delta v)}{N_{\text{ran}}(\Delta v)} - 1, \quad (9)$$

where  $N_{\text{obs}}$  and  $N_{\text{ran}}$  are the normalized number of absorption component pairs with a given velocity separation per  $\Delta v$  (Kerscher, Szapudi, & Szalay 2000) and where the velocity separation ( $z_1 > z_2$ ) is defined rela-

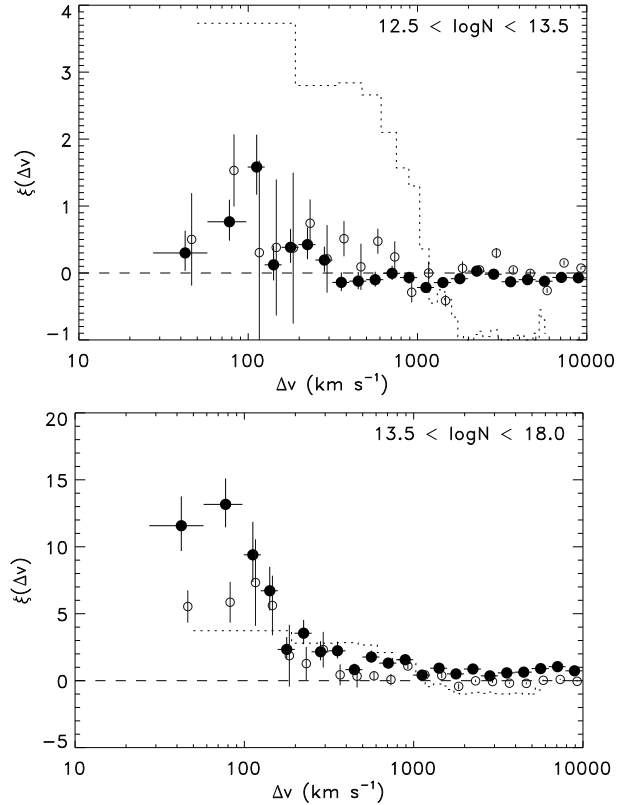


FIG. 17.— Variation in TPCF with component strength. Weak H I absorbers (top,  $12.5 < \log N < 13.5$ ) show only modest clustering, while stronger Ly $\alpha$  components (bottom,  $\log N > 13.5$ ) show significant clustering at  $\Delta v \sim 50 - 300 \text{ km s}^{-1}$ . The same trend is apparent in the *HST*/STIS absorbers from Tilton et al. (2012) (open circles). Dotted lines show the galaxy-galaxy TPCF of Penton, Stocke, & Shull (2004).

tivistically

$$\frac{\Delta v}{c} \equiv \frac{(1+z_1)^2 - (1+z_2)^2}{(1+z_1)^2 + (1+z_2)^2}. \quad (10)$$

The observed redshifts ( $z_1, z_2$ ) are taken as any pair of Ly $\alpha$  components in the same sight line detected at  $\geq 4\sigma$ . For simplicity, and to avoid spurious clustering signal from velocity mis-matches between lines in different transitions, we use only Ly $\alpha$  components, not systems in which different closely-spaced components may be grouped together into the same system. In principle, any absorption component could be used. See Labatie et al. (2010) and references therein for a discussion of biases inherent to this and other estimators of the TPCF.

The random absorber distribution is calculated with a Monte-Carlo simulation using the detailed fit to the observed IGM detection statistics and the actual data in each of the survey sight lines. Random component locations are simulated 100 times in each sight line. A similar technique was used by Penton, Shull, & Stocke (2000) and Penton, Stocke, & Shull (2004) to simulate absorbers in *HST*/FOS and STIS data. At each resolution element  $\Delta v$  in each sight line, we calculate the  $4\sigma$  minimum equivalent width detection supported by the  $S/N$  of the data. The  $W_{\text{min}}(\lambda)$  vector is converted to  $N_{\text{Ly}\alpha, \text{min}}(z)$  and the probability of finding a component

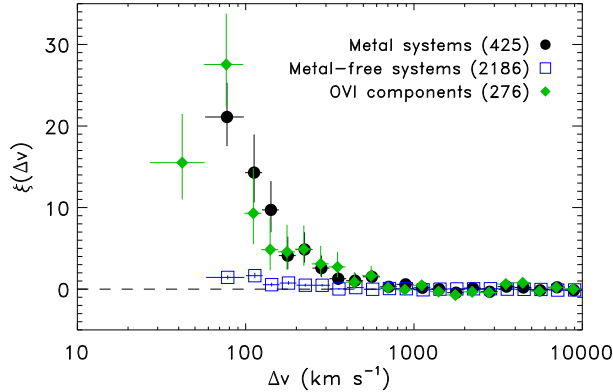


FIG. 18.— Two-point correlation function of metal/non-metal absorbers. IGM systems with absorption in at least one metal ion (black filled circles) show a strong TPCF signal at  $\Delta v \sim 100 \text{ km s}^{-1}$ , while H I-only systems (open squares) show little or no signal. O VI  $\lambda 1032$  components (green diamonds) show a similar TPCF behavior to metal-bearing HI systems.

in velocity resolution element  $dv$  is given from Eq. (7) as

$$P_{\text{ran}}(z) = C_0 \frac{dv}{c} (1+z)^\gamma \quad (11)$$

$$\times \left[ \left( \frac{N_{\text{min}}(z)}{10^{14} \text{ cm}^{-2}} \right)^{-\beta} - \left( \frac{N_{\text{max}}(z)}{10^{14} \text{ cm}^{-2}} \right)^{-\beta} \right].$$

Integrated over the Ly $\alpha$  pathlength in each component,  $P_{\text{ran}}(z)$  should equal the number of observed Ly $\alpha$  systems in that sight line, modulo cosmic variance. If the probability at a given resolution element is greater than a randomly generated number, an absorption component is placed at this redshift position. When the entire redshift pathlength of the sight line has been processed, the number of pairs in the randomly-distributed components is found, and the result  $N_{\text{ran}}(\Delta v)$  is added to a list of random pairs. We produce strong and weak pairs by setting limits on  $N_{\text{min}}$  and  $N_{\text{max}}$  in both the observed and artificial component lists.

Figure 16 shows the behavior of the observed and random component pairs, normalized to the velocity width in each bin in our sample (top panel). As expected, the distribution of random pairs is flat as a function of  $\Delta v$ . The observed pairs show a significant peak at  $50 \lesssim \Delta v \lesssim 300 \text{ km s}^{-1}$ . The two-point correlation function (lower panel) shows a significant correlation at  $\Delta v \lesssim 300 \text{ km s}^{-1}$  and no signal at much higher velocities. This is in contrast to the galaxy-galaxy TPCF (dotted) from Penton, Stocke, & Shull (2004) which shows significant correlation at  $\Delta v < 1000 \text{ km s}^{-1}$  and significant anticorrelation at  $\Delta v > 1000 \text{ km s}^{-1}$ . Whether this anticorrelation is due to the presence of voids in the galaxy distribution, or is an artifact of the TPCF methodology (Kaiser 1987) is unknown. We note that the random absorber population (responsible for the denominator in  $\xi$ ) is extremely sensitive to the fit parameters assumed for the Ly $\alpha$  forest and its evolution. This introduces a small uncertainty in the scaling of the  $\xi$ , but it does not change the overall flat nature of  $N_{\text{ran}}(\Delta v)$  seen in the top panel of Figure 16.

Splitting the TPCF into strong and weak subsamples

(Figure 17), we see that the strong components ( $\log N > 13.5$ ) show signal equal to or stronger than the galaxy-galaxy TPCF at  $\Delta v \sim 100 \text{ km s}^{-1}$ , while the weaker components ( $12.5 \leq \log N < 13.5$ ) show a much smaller clustering signal. This is in keeping with the picture of strong H I systems in and around galaxy halos, which are clustered (Rudie et al. 2013), or at least associated with large-scale structures such as filaments. Neither strong nor weak samples show significant TPCF at  $300 \lesssim \Delta v \lesssim 1000 \text{ km s}^{-1}$  where the galaxies are still highly clustered ( $\xi \gtrsim 3$ ).

The decrease in  $\xi$  at  $\Delta v < 60 \text{ km s}^{-1}$  shown in Figures 16 and 17 is intriguing. The velocity resolution of COS ( $\sim 17 \text{ km s}^{-1}$ ) and the typical width of Ly $\alpha$  lines ( $b \sim 33 \text{ km s}^{-1}$ ,  $FWHM \sim 55 \text{ km s}^{-1}$ ) suggest that the low  $\xi$  values in the lowest-velocity bins may be due to finite instrumental resolution, line blending, and related systematic effects. Post-processing the Tilton et al. (2012) catalog of *HST*/STIS absorbers shows a similar turn-down at low velocities (open circles in Figures 16 and 17). Since the resolution of the STIS/E140M grating is  $\sim 7 \text{ km s}^{-1}$  (compared with  $\sim 17 \text{ km s}^{-1}$  for the medium-resolution COS gratings), this hints that the downturn at  $\Delta v < 100 \text{ km s}^{-1}$  may be a real effect. If real, this lack of correlation at the smallest velocities may be indicative of the kinematics within galaxy halos. However, differentiating blended components, especially in strong absorbers, is subject to quite a bit of systematic uncertainty and we view this apparent downturn in  $\xi$  at the smallest  $\Delta v$  as suggestive only. Unfortunately, resolution limitations restrict the ability of modern cosmological simulations to track such small velocity separations (e.g., Cen & Chisari 2011).

At smaller velocity separations, line blending introduces uncertainties and biases into our ability to separate and identify velocity components. The median doppler parameters of H I and O VI absorbers are comparable, at  $\langle b \rangle \approx 30 \text{ km s}^{-1}$ , and the full width at half maximum,  $\Delta v_{FWHM} \approx 1.67b$  is approximately  $50 \text{ km s}^{-1}$ . We therefore distrust any TPCF signal at those separations.

Next, we investigate the clustering properties of IGM systems with and without metal-ion absorption. We approach this in two ways. First, we analyze IGM systems rather than the individual Ly $\alpha$  components studied above, so that metal absorption can more easily be associated with H I columns despite small velocity uncertainties. Since systems have a minimum velocity half-width of  $30 \text{ km s}^{-1}$  and many systems (particularly metal systems) are broader than this, we restrict this analysis to velocity separations  $\Delta v > 60 \text{ km s}^{-1}$ . To generate a TPCF, we assume that the distribution of randomly-placed systems in both metal and non-metal systems is flat with  $\Delta v$ , as in the top panel of Figure 16, and that there is no clustering at  $\Delta v > 1000 \text{ km s}^{-1}$ . Secondly, in order to eliminate bias due to system definitions, we investigate the clustering of metal-ion components themselves using the most commonly-seen transition (O VI  $\lambda 1032$ ). This method is analogous to the Ly $\alpha$  TPCF shown in Figure 16. Again, we assume a flat distribution of randomly placed absorbers in each case.

Figure 18 shows the clustering properties of the non-metal systems (open circles) along with the metal systems. Individual metal component clustering is shown

in the various colored symbols. The metal component sample sizes are quite a bit smaller than the H I sample or even the metal/non-metal system samples, and thus the uncertainties are much larger. However, O VI  $\lambda 1032$  components show a clustering signal at  $\Delta v \approx 100 \text{ km s}^{-1}$  which is considerably stronger than that seen in the metal systems. This difference may be a result of our process of system definition: in many cases, closely-spaced metal components are grouped together into a single system which will systematically reduce the number of absorber pairs at close velocity separation.

Qualitatively, metal-ion components and metal-bearing systems show strong clustering ( $\xi \sim 10 - 50$ ) peaked at  $\Delta v \sim 50 - 200 \text{ km s}^{-1}$ , albeit with substantial uncertainty due to the small size of the samples. Pieri et al. (2014) see a similar trend in a large sample of Ly $\alpha$  absorbers at  $2.4 < z < 3.1$  in the BOSS survey, with a high degree of clustering and correlation of metal absorbers at scales down to  $\Delta v \approx 130 \text{ km s}^{-1}$  (the resolution limit of their data). The non-metal systems show a peak  $\xi \lesssim 1$  at the same velocity range. This suggests that most of the radial-velocity clustering in the IGM can be attributed to strong, metal-bearing systems in the CGM, again consistent with the picture of strong, metal-enriched absorption being associated with galaxy halos.

## 6. SUMMARY OF PRIMARY RESULTS

We present a high-quality, medium-resolution HST/COS survey of the IGM along 82 UV-bright AGN sight lines. Because the sight lines were chosen for sensitivity to weak IGM absorbers at low-redshift over the maximum pathlength, we favor targets observed with both the COS/G130M and G160M gratings with a typical  $S/N \gtrsim 15$  per resolution element. We limit the redshifts of the AGN to  $0.05 < z_{\text{AGN}} < 0.85$  to maximize IGM pathlength for species of interest (H I, O VI, etc.) while minimizing line confusion.

The spectra were processed with semi-automated continuum fitting and line-finding/measurement routines to minimize the subjective bias associated with many previous IGM surveys. The identity of absorption features is established through a manual process and lines are remeasured as necessary. Galactic, instrumental, and probable AGN-intrinsic features are flagged. In total, 5138 individual lines are identified as absorption from intervening material in the IGM. This includes 4234 Ly $\alpha$  lines, 606 Ly $\beta$  lines, and 1633 metal-ion lines representing 25 metal ion species. The median and  $\pm 1\sigma$  redshift of absorption systems is  $z = 0.14_{-0.10}^{+0.18}$ .

To better facilitate comparisons between species at the same redshift, the IGM lines are grouped by into 2611 distinct redshift systems of which 418 are detected in at least one metal line. The most common metal species is O VI (present in 280 systems) followed by C III (115), Si III (123), C IV (70), and N V (59). Ne VIII is only detected at a significant level in three systems.

We present below a summary of our primary science results:

- The fraction of IGM H I systems detected in one or more metal ions is a strong function of  $N_{\text{HI}}$ . Metals are rarely (less than 10%) detected in  $N_{\text{HI}} \lesssim 10^{13.5} \text{ cm}^{-2}$  absorbers, but become nearly ubiqui-

tous for strong systems ( $N_{\text{HI}} \gtrsim 10^{15} \text{ cm}^{-2}$ ).

- The cumulative distribution of H I absorbers at  $z \leq 0.47$  in the sample (Figure 5) follows a power law in H I column density of the form  $dN(> N)/dz = C_{14} (N/10^{14} \text{ cm}^{-2})^{-(\beta-1)}$  over the column density range  $12 \leq \log N_{\text{HI}} \leq 17$  with normalization  $C_{14} = 25 \pm 1$  and differential index  $\beta = 1.65 \pm 0.02$ .
- Dividing the sample into redshift bins of  $\Delta z \approx 0.1$  and analyzing the subsamples, we see clear evolution in both the slope  $\beta$  and normalization  $C_{14}$  of the distribution. We parameterize the evolution of the diffuse IGM H I absorbers as  $dN(> N)/dz = C_0 (1+z)^\gamma (N/10^{14} \text{ cm}^{-2})^{-[\beta(z)-1]}$  with  $C_0 = 16 \pm 1$ ,  $\gamma = 2.3$ , and  $\beta(z) = (1.75 \pm 0.03) - (0.31 \pm 0.10)z$  for  $z \leq 0.47$ .
- Metal systems analyzed in the same manner as H I suggest that O VI evolves in the same sense as H I with  $\gamma \sim 1.8 \pm 0.8$ . Smaller samples of N V, C III, and Si III absorbers do not present clear evidence for evolution.
- We calculate the contribution to the closure density by a particular species,  $\Omega_{\text{ion}}$ , and the contribution represented by gas which is traced by a particular species,  $\Omega_{\text{IGM}}^{(\text{ion})}$ . The values given in Table 6 are consistent with previous surveys.
- A two-point correlation function (TPCF) of Ly $\alpha$  components shows that there is significant clustering of IGM absorbers in radial velocity. Figure 16 shows a significant clustering signal at  $\Delta v = 60 - 300 \text{ km s}^{-1}$  and little or no signal at higher velocities. This is in contrast to the galaxy-galaxy radial velocity clustering found by Penton, Stocke, & Shull (2004) which shows significant clustering at  $\Delta v < 1000 \text{ km s}^{-1}$ . Dividing the sample into strong ( $\log N_{\text{HI}} > 13.5$ ) and weak ( $\log N_{\text{HI}} < 13.5$ ) absorbers, we see that nearly all of the clustering signal is accounted for by the stronger systems. Examining metal and non-metal systems reveals an extremely strong TPCF for metal systems as well as in components of common metal-ion transitions (O VI 1032 Å, etc.)

This paper represents many years of work by the COS Science Team to characterize the baryon content, structure, and metallicity of the low-redshift IGM. At this point, it is worth summarizing the status of low-redshift IGM surveys and models: What properties of the IGM are now well established? What are the remaining uncertainties? Where are avenues for future observations and theoretical work? The COS (G130M/G160M) spectra had resolving power  $R \approx 18,000$  and identified  $\sim 2600$  IGM absorbing system and 418 metal-line systems (280 O VI, 70 C IV). The total redshift path length,  $\Delta z = 21.7$ , is four times larger than our previous low-redshift surveys with STIS (Danforth & Shull 2008; Tilton et al. 2012) which identified 650-750 Ly $\alpha$  absorbers. For comparison, the Quasar Absorption Line Survey HST/FOS Key Project (Jannuzi et al. 1998) observed 83 AGN sight lines. Although the FOS survey covered a larger path length,  $\Delta z \approx 49$ , its line sample was smaller, with 1129

$\text{Ly}\alpha$  lines, 107 C IV systems, and 41 O VI systems, and the spectra were obtained at an order-of-magnitude lower resolution ( $R \approx 1300$ ).

With the larger COS medium-resolution IGM survey, the bivariate distribution of H I absorbers,  $f(N_{\text{HI}}, z)$ , is now well established at redshifts  $z \leq 0.4$ . Its parameterization in column density and redshift are fitted to the form  $N_{\text{HI}}^{-\beta}(1+z)^\gamma$ , with a differential low-redshift slope of  $\beta = 1.65 \pm 0.02$  over the range  $12 < \log N_{\text{HI}} < 17$ , identical to the slope at  $\langle z \rangle = 2.4$  found by the Keck Baryonic Structure Survey for  $\text{Ly}\alpha$  absorbers with  $\log N_{\text{HI}} > 13.5$ . (An earlier survey with VLT/UVES by Kim et al. (2002) found  $\beta \approx 1.5$  over the range  $1.5 < z < 4.0$ .) The COS survey has also established that strong H I absorbers evolve faster than weak absorbers, with redshift-evolution indices  $\gamma_{\text{weak}} = 1.15 \pm 0.05$  for  $13 < \log N_{\text{HI}} < 14$  and  $\gamma_{\text{strong}} = 2.3 \pm 0.1$  for  $\log N_{\text{HI}} > 14$ . However, for the low column density absorbers, the  $dN/dz$  values determined in this work are somewhat too high to join seamlessly with the higher redshift line densities found from ground-based spectroscopy using the slopes obtained by both the COS and ground-based studies. For the higher column density absorbers, a slope change is *required* somewhere between  $0.4 \lesssim z \lesssim 2$ . The evolution of the IGM cannot be well-understood at all cosmic epochs simply by interpolating between the the low ( $z \lesssim 0.4$ ) and high redshift ( $z \gtrsim 2$ ) regimes.

For the cosmological baryon census, the COS survey confirms previous studies (Shull, Smith, & Danforth 2012; Tilton et al. 2012) which found that  $\sim 20 - 25\%$  of the baryons reside in the intergalactic  $\text{Ly}\alpha$  forest, ranging in column density from  $12.8 < \log N_{\text{HI}} < 16.0$ . Additional matter exists in higher column density systems, extending up to  $\log N_{\text{HI}} \approx 19$  (Penton, Stocke, & Shull 2004). With nearly 2600 H I absorbers, the COS survey provides better statistics. Some uncertainties remain for weak  $\text{Ly}\alpha$  lines with equivalent widths  $W_\lambda < 30 \text{ m}\text{\AA}$  ( $\log N_{\text{HI}} < 12.74$ ) and for rare high-column density systems. For strong absorbers ( $\log N_{\text{HI}} > 15$ ) our survey typically has fewer than 10  $\text{Ly}\alpha$  lines per column density bin ( $\Delta \log N = 0.2$ ). In addition, the ionization corrections required to convert the absorber distribution,  $f(N_{\text{HI}}, z)$ , into a baryon density parameter,  $\Omega_b$ , involve uncertain physical parameters such as the ionizing UV background and hydrogen photoionization rate

( $\Gamma_H$ ), characteristic absorbers sizes, and cloud temperature. In fact, the column density distribution of  $\text{Ly}\alpha$  absorbers can be used, together with cosmological simulations, to constrain the amplitude of the low-redshift ionizing background (Kollmeier et al. 2014; Shull et al. 2015).

Further progress in characterizing the evolution of structure in the low-redshift IGM will likely occur along several fronts. First, we need to characterize the H I distribution at the low-column end, searching for the expected turnover in the distribution below  $\log N_{\text{HI}} < 12.4$ . This will require high-S/N data to measure  $\text{Ly}\alpha$  equivalent widths down to  $5 \text{ m}\text{\AA}$  ( $\log N_{\text{HI}} \approx 12.0$ .) Second, we have little knowledge of the evolution of the IGM between  $z \approx 1.5$  and  $z \approx 0.4$ , the epoch when physical conditions change rapidly as star-formation rates decline. Probing the IGM beyond  $z > 0.4$  will require extensive surveys in the “near-ultraviolet desert” ( $\lambda > 1700 \text{ \AA}$ ), both for  $\text{Ly}\alpha$  absorbers as well as key lines of carbon, oxygen, nitrogen, and silicon that measure the extent of metal transport from galaxies into the IGM.

It is our pleasure to acknowledge fruitful discussions with many colleagues during the course of this work including Ben Oppenheimer, Devin Silvia, and Joshua Moloney. Julie Davis (Colorado), Alex Filippenko, Brad Cenko, Weidong Li, Weikang Zhang (U. C. Berkeley), Meg Urry, Erin Bonning Wells, and Jedidah Isler (Yale) were instrumental in the acquisition of several of the datasets used in this study. We also acknowledge the valuable contributions made by our anonymous referee who provided the thorough, critical, expert review and lead to a much-improved scientific paper. This work was supported by NASA grants NNX08AC14G (COS Science Team), HST-AR-1243.06, HST-GO-12612.01-A, and HST-GO-13008.01-A to the University of Colorado at Boulder. BAK and JTS acknowledge support from NSF grant AST1109117. JMS acknowledges NSF grant AST07-07474 and thanks the Institute for Astronomy at Cambridge University for support as a Sackler Visiting Lecturer. Scott Fleming at MAST was instrumental in the production of the High-Level Science Products associated with this survey. The authors made extensive use of the MAST, NED, and ADS Archives during this work.

*Facility: HST (COS), FUSE, HST (STIS)*

## REFERENCES

- Bahcall, J. N., Boksenberg, A., Hartig, G. F., et al. 1993, *ApJS*, 87, 1  
 Bahcall, J. N., Bergeron, J., Boksenberg, A., et al. 1996, *ApJ*, 457, 19  
 Bahcall, J. M., & Peebles, J. 1969, *ApJ*, 156, L7  
 Bordoloi, R., Tumlinson, J., Werk, J. K., Oppenheimer, B. D., Peeples, M. S., Prochaska, J. X., Tripp, T. M., Katz, N., et al., 2014, *ApJ*, 796, 136  
 Cen, R. & Chisari, N. E., 2011, *ApJ*, 731, 11  
 Cen, R., & Fang, T. 2006, *ApJ*, 650, 573  
 Chen, H.-W., & Mulchaey, J. 2009, *ApJ*, 701, 1219  
 Danforth, C. W., & Shull, J. M. 2005, *ApJ*, 624, 555  
 Danforth, C. W., Shull, J. M., Rosenberg, J. L., & Stocke, J. T. 2006, *ApJ*, 640, 205  
 Danforth, C. W., & Shull, J. M. 2008, *ApJ*, 679, 194  
 Danforth, C. W. 2009, *AIP Conf. Proc.* 1135, 8, eds. G. Sonneborn, M. E. van Steenberg, H. W. Moos, & W. P. Blair (arXiv:0812.0602)  
 Danforth, C. W., Stocke, J. T., & Shull, J. M., 2010a, *ApJ*, 710, 613  
 Danforth, C. W., Keeney, B. A., Stocke, J. T., Shull, J. M., & Yao, Y. 2010b, *ApJ*, 720, 976  
 Danforth, C. W., Nalewajko, K., France, K., & Keeney, B. A., 2013, *ApJ*, 764:57  
 Davé, R., Oppenheimer, B. D., Katz, N., Kollmeier, J. A., & Weinberg, D. H., 2010, *MNRAS*, 408, 2051  
 Davé, R., & Tripp, T. M. 2001, *ApJ*, 553, 528  
 Dunn, J. P., Crenshaw, D. M., Kraemer, S. B., & Gabel, J. R., 2007, *AJ*, 134, 1061  
 Fedchak, J. A., Wiese, L. M., & Lawler, J. E., 2000, *ApJ*, 538, 773  
 Fox, A. J., Bordoloi, R., Savage, B. D., Lockman, F. J., Jenkins, E. B., Wakker, B. P., Bland-Hawthorn, J., Hernandez, S., et al., 2015, *ApJ*, 799, 7  
 Frank, S., Rasera, Y., Vibert, D., et al. 2012, *MNRAS*, 420, 1731  
 Ganguly, R., Lynch, R. S., Charlton, J. C., et al. *MNRAS*, 435, 1233  
 Gehrels, N. 1986, *ApJ*, 303, 336  
 Green, J. C., Froning, C. S., Osterman, S., et al. 2012, *ApJ*, 744, 60  
 Hussain, T., Muzahid, S., Narayanan, A., Srianand, R., Wakker, B. P., Charlton, J. C., Pathak, A., 2015, *MNRAS*, 446, 2444

- Janknecht, E., Reimers, D., Lopez, S., & Tytler, D., 2006, *A&A*, 458, 427
- Jannuzi, B. T., et al. 1998, *ApJS*, 118, 1
- Jenkins, E. & Tripp, T. M., 2001, *ApJS*, 137, 297
- Jenkins, E. & Tripp, T. M., 2006, *ApJ*, 637, 548
- Jenkins, E. & Tripp, T. M., 2011, *ApJ*, 734, 65
- Johnson, S. D., Chen, H.-W., & Mulchaey, J. S., 2015, *MNRAS*, 449, 3263
- Kaiser, N., 1987, *MNRAS*, 227, 1
- Keeney, B. A., Danforth, C. W., Stocke, J. T., France, K., & Green, J. C. 2012, *PASP*, 124, 830
- Kelleher, D. E., & Podobedova 2008, *J. Phys. Chem. Ref. Data*, 37, 267
- Kerscher, M., Szapudi, I., & Szalay, A. S., 2000, *ApJ*, 535, 13
- Kim, T.-S., Carswell, R. F., Cristiani, S., D’Odorico, S. & Giallongo, E., 2002, *MNRAS*, 335, 555
- Kirkman, D., Tytler, D., Lubin, D., & Charlton, J., 2007, *MNRAS*, 376, 1227
- Kollmeier, J. A., Weinberg, D. H., Oppenheimer, B. D., et al. 2014, *ApJ*, 789, L32
- Kriss, G. A. 2011, COS Instrument Science Report 2011-01(v1), Improved Medium Resolution Line Spread Functions for COS FUV Spectra (Baltimore: STScI)
- Labatie, A., Starck, J.-L., Lachière-Rey, M., & Arnalte-Mur, P., 2010, *ArXiv*, 1009.1232
- Larson, D., Dunkley, J., Hinshaw, G., et al. 2011, *ApJS*, 192, 16
- Lehner, N., Savage, B. D., Richter, P., Sembach, K. R., Tripp, T. M., & Wakker, B. P. 2007, *ApJ*, 658, 680
- Martin, D. C., Chang, D., Matuszewski, M., Morrissey, P., Rahman, S., Moore, A., & Steidel, C. C., 2014a, *ApJ*, 786, 106
- Martin, D. C., Chang, D., Matuszewski, M., Morrissey, P., Rahman, S., Moore, A., Steidel, C. C., & Matsuda, Y., 2014b, *ApJ*, 786, 107
- Meiring, J. D., Tripp, T. M., Werk, J. K., et al. 2013, *ApJ*, 767, 49
- Morton, D. C., York, D. G., & Jenkins, E. B., 1988, *ApJS*, 68, 449
- Morton, D. C. 2003, *ApJS*, 149, 205
- Muzahid, S., Kacprzak, G. G., Churchill, C. W., Charlton, J. C., Nielsen, N. M., Mathes, N. L., & Trujillo-Gomez, S., 2015, *ApJ*, 811, 132
- Narayanan, A., Wakker, B. P. & Savage, B. D. 2009, *ApJ*, 703, 74
- Narayanan, A., Savage, B. D., Wakker, B. P., et al. 2011, *ApJ*, 730:15
- Oppenheimer, B. D., & Davé, R. 2008, *MNRAS*, 383, 577
- Osterman, S., Green, J., Froning, C., et al. 2011, *Ap&SS*, 335, 257
- Peebles, P. J. E., 1980, *The Large-Scale Structure of the Universe*, Princeton University Press.
- Penton, S. V., Stocke, J. T., & Shull, J. M. 2000, *ApJS*, 130, 121
- Penton, S. V., Shull, J. M., & Stocke, J. T. 2000, *ApJ*, 544, 150
- Penton, S. V., Stocke, J. T., & Shull, J. M. 2004, *ApJS*, 152, 29
- Pieri, M. M., Mortonson, M. J., Frank, S., et al. 2014, *MNRAS*, 441, 1718
- Press, W. H., Teukolsky, S. A., Vetterling, W. T., & Flannery, B. P., 1992, “Numerical Recipes in C. The Art of Scientific Computing”, Cambridge: University Press
- Prochaska, J. X., Weiner, B., Chen, H.-W., Mulchaey, J., & Cooksey, K., 2011, *ApJ*, 740, 91
- Ribaudo, J., Lehner, N., & Howk, J. C., 2011, *ApJ*, 736, 42
- Richter, P., Savage, B. D., Sembach, K. R., & Tripp, T. M. 2006, *A&A*, 445, 827
- Rudie, G. C., Steidel, C. C., Shapley, A. E., & Pettini, M., 2013, *ApJ*, 769, 146
- Savage, B. D., Lehner, N., Wakker, B. P., Sembach, K. R., & Tripp, T. M. 2005, *ApJ*, 626, 776
- Savage, B. D., Narayanan, A., Wakker, B. P., Stocke, J. T., Keeney, B. A., Shull, J. M., Sembach, K. R., Yao, Y., & Green, J. C., 2010, *ApJ*, 719, 1526
- Savage, B. D., Lehner, N., & Narayanan, A., 2011, *ApJ*, 743:180
- Savage, B. D., Kim, T.-S., Wakker, B. P., et al. 2014, *ApJS*, 212, 8
- Schneider, D. P., Hartig, G. F., Jannuzi, B. T., et al. 1993, *ApJS*, 87, 45
- Sembach, K. R., Howk, J. C., Savage, B. D., Shull, J. M., & Oegerle, W. E., 2001, *ApJ*, 561, 573
- Shull, J. M., Giroux, M. L., Penton, S. V., et al. 2000, *ApJ*, 538, L13
- Shull, J. M., Moloney, J., Danforth, C. W., & Tilton, E. 2015, *ApJ*, 811, 3
- Shull, J. M. 2014, *ApJ*, 784, 142
- Shull, J. M., Danforth, C. W. & Tilton, E. 2014, *ApJ*, 796, 44
- Shull, J. M., Smith, B. D., & Danforth, C. W., 2012, *ApJ*, 759, 23
- Shull, J. M., Stevans, M., & Danforth, C. W. 2012, *ApJ*, 752, 162
- Smith, B. D., Hallman, E. J., Shull, J. M., & O’Shea, B. W., 2011, *ApJ*, 731:6
- Steidel, C. C., Bogosavljević, M., Shapley, A. E., Kollmeier, J. A., Reddy, N. A., Erb, D. K., & Pettini, M., 2011, *ApJ*, 736, 160
- Stevans, M., Shull, J. M., Danforth, C. W., & Tilton, E. 2014, *ApJ*, 794, 75
- Stocke, J. T., Penton, S. V., Danforth, C. W., Shull, J. M., Tumlinson, J., & McLin, K. M. 2006, *ApJ*, 641, 217
- Stocke, J. T., Keeney, B. A., Danforth, C. W., Shull, J. M., Froning, C. S., Green, J. C., Penton, S. V. & Savage, B. D., 2013, *ApJ*, 763, 148
- Stocke, J. T., Keeney, B. A., Danforth, C. W., et al. 2014, *ApJ*, 791, 128
- Thom, C., & Chen, H.-W. 2008, *ApJ*, 683, 22
- Tilton, E. M., Danforth, C. W., Shull, J. M., & Ross, T. L. 2012, *ApJ*, 759, 112
- Toner, A., & Hibbert, A., 2005, *MNRAS*, 361, 673
- Tripp, T. M., Giroux, M. L., Stocke, J. T., Tumlinson, J., & Oegerle, W. R., 2001, *ApJ*, 563, 724
- Tripp, T. M., Sembach, K. R., Bowen, D. V., Savage, B. D., Jenkins, E. B., Lehner, N., & Richter, P. 2008, *ApJS*, 177, 39
- Tripp, T. M., Meiring, J. D., Prochaska, J. X., Willmer, C. N. A., Howk, J. C., Werk, J. K., Jenkins, E. B., Bowen, D. V., Lehner, N., Sembach, K. R., Thom, C., & Tumlinson, J., 2011, *Science*, 334, 952
- Tumlinson, J., Thom, C., Werk, J. K., et al. 2011, *Science*, 334, 948
- Tumlinson, J., Thom, C., Werk, J. K., et al. 2013, *ApJ*, 777, 59
- Wakker, B. P., Hernandez, A. K., French, D., Kim, T.-S., Oppenheimer, B. D., & Savage, B. D., 2015, *arXiv:1504.02539*
- Werk, J. K., Prochaska, J. X., Tumlinson, J., Peebles, M. S., Tripp, T. M., Fox, A. J., Lehner, N., Thom, C., O’Meara, J. M., et al. 2014, *ApJ*, 792, 8
- Weymann, R. J., Rauch, M., Williams, R., et al. 1995, *ApJ*, 561, 573
- Weymann, R. J., Jannuzi, B. T., Lu, L., et al. 1998, *ApJ*, 506, 1